



**Politecnico  
di Torino**

**Politecnico di Torino**

Corso di Laurea in Ingegneria Aerospaziale

A.A. 2020/2021

Sessione di Laurea Luglio 2021

# **Hydrodynamic stability and transition to turbulence in pulsatile flows**

**Relatore:**

Prof.ssa Stefania Scarsoglio

**Candidato:**

Gianluca Zufferli

<b>SUMMARY</b>	1
<b>1. INTRODUCTION</b>	2
1.1 REYNOLDS NUMBER	2
1.2 WOMERSLEY NUMBER	2
1.3 PIPE FLOW (HAGEN-POISEUILLE FLOW)	2
1.4 TRANSITION OF PULSATILE FLOW	4
1.4.1 LAMINAR FLOW	4
1.4.2 TRANSITION OF STEADY FLOW	5
1.4.3 TRANSITION OF UNSTEADY FLOW	6
1.5 PHASE-LOCKED TURBULENCE	9
<b>2. EXPERIMENTS AND NUMERICAL SIMULATIONS</b>	13
2.1 XU <i>ET AL.</i> EXPERIMENT N°1	13
2.1.1 EXPERIMENT'S SET UP	13
2.1.2 RESULTS	14
2.1.3 DISCUSSION	17
2.2 XU <i>ET AL.</i> EXPERIMENT N°2	20
2.2.1 PUFF TURBULENCE	20
2.2.2 HELICAL INSTABILITY	22
2.2.3 HELICAL INSTABILITY IN SIMULATION	23
2.2.4 LUMEN CONSTRICTION	25
2.2.5 BLOOD FLOW EXPERIMENTS	26
2.3 TRANSIENT GROWTH NUMERICAL SIMULATIONS	26
<b>3. CONCLUSIONS</b>	29
<b>4. BIBLIOGRAPHY</b>	31

## SUMMARY

As reported in the introduction of the study conducted by Trip *et al.* [1], the transition of a pulsatile flow from the laminar to the turbulent regime has been deeply analyzed primarily because of the main question concerning the possibility of transition to turbulence of the flow in the cardiovascular system, in particular in large arteries (either under normal conditions or due to physical exercise or diseases). Mentioning what was stated by Stein and Sabbah [2], turbulent flow, or more generally “disturbed flow”, and the resulting fluctuating wall shear stresses have been associated with the etiology of a range of cardiovascular diseases. In fact, it is possible that in some fractions of the cycle the instantaneous Reynolds number is particularly high, and this parameter is such as to induce the average flow in the large arteries in the transition regime. Since it would be too complicated to deal with this problem considering the biomechanical geometry entirely, to facilitate the discussion, attention has been paid to the study of the simplified problem of the transition of a pulsatile flow in a straight, rigid pipe. Effects due to, for instance, vessel curvature, bifurcations, wall distention, wall roughness, and non-Newtonian behavior of blood are thus ignored. This isolates the core fundamental fluid mechanical problem, which is closely linked to the research of transition of steady pipe flow. [1]

In the first part are mentioned concepts of relevant parameters (such as Reynolds and Womersley numbers), pipe flow generalities, the transition of a pulsatile flow (laminar, steady and unsteady) and the phenomenon of phase-locked turbulence.

The second part presents the experiments carried out to visualize how a pulsatile flow reacts to the change of determined parameters and to evaluate the modalities and consequences of the transition to turbulence of pulsatile flow. Furthermore, it is analyzed the role of the transition growth in the transition to turbulence.

# 1. INTRODUCTION

## 1.1 REYNOLDS NUMBER

The Reynolds number describes the ratio of inertial to viscous forces. It is a dimensionless number used to categorize the fluids systems in which the effect of viscosity is important in controlling the velocities or the flow pattern of a fluid. If the axial velocity  $u$  is composed of a steady velocity component  $u_s$  and an oscillatory velocity component  $u_o$ , it is possible to define the mean Reynolds number  $Re_m \equiv 2u_s R/\nu$  and the oscillatory Reynolds number  $Re_o \equiv 2u_o R/\nu$ . In these definitions,  $R$  is the radius of the pipe and  $\nu$  the kinematic viscosity ( $\nu = \mu/\rho$  where  $\mu$  is the dynamic viscosity and  $\rho$  the fluid density). Considering a fluid flow in a pipe, the Reynolds number has a particular importance because if  $Re < 2300$  the flow is laminar, otherwise if  $Re > 2300$  the flow becomes turbulent.

The ratio  $Re_o/Re_m$  is also commonly used. This parameter describes the ratio of oscillating and mean velocity component.

## 1.2 WOMERSLEY NUMBER

The Womersley number is a dimensionless number used in biofluid mechanics and biofluid dynamics as an expression of the pulsatile flow frequency in relation to viscous effects, in other words it gives the ratio of transient inertial force to viscous forces. Mathematically, it is expressed as  $\alpha \equiv Wo = R\sqrt{\omega/\nu}$ , where  $R$  is the radius of the pipe,  $\nu$  the kinematic viscosity and  $\omega = 2\pi f$  the angular velocity ( $f$  is the frequency of the oscillation). This parameter is important in keeping dynamic similarity when scaling an experiment. The Womersley number is also important in determining the thickness of the boundary layer to see if the entrance effects can be ignored.

## 1.3 PIPE FLOW (HAGEN-POISEUILLE FLOW)

*Navier-Stokes equations for an incompressible fluid with constant properties in cylindrical coordinates, with  $\mathbf{V} = v_r \mathbf{e}_r + v_\theta \mathbf{e}_\theta + v_z \mathbf{e}_z$ , are written as*

$$\frac{\partial v_r}{\partial r} + \frac{v_r}{r} + \frac{1}{r} \frac{\partial v_\theta}{\partial \theta} + \frac{\partial v_z}{\partial z} = 0, \quad (1)$$

$$\frac{\partial v_r}{\partial t} + v_r \frac{\partial v_r}{\partial r} + \frac{v_\theta}{r} \frac{\partial v_r}{\partial \theta} + v_z \frac{\partial v_r}{\partial z} - \frac{v_\theta^2}{r} = -\frac{1}{\rho} \frac{\partial p}{\partial r} + \nu \left( \nabla^2 v_r - \frac{v_r}{r^2} - \frac{2}{r^2} \frac{\partial v_\theta}{\partial \theta} \right), \quad (2)$$

$$\frac{\partial v_\theta}{\partial t} + v_r \frac{\partial v_\theta}{\partial r} + \frac{v_\theta}{r} \frac{\partial v_\theta}{\partial \theta} + v_z \frac{\partial v_\theta}{\partial z} + \frac{v_r v_\theta}{r} = -\frac{1}{\rho r} \frac{\partial p}{\partial \theta} + \nu \left( \nabla^2 v_\theta + \frac{2}{r} \frac{\partial v_r}{\partial \theta} - \frac{v_\theta}{r^2} \right), \quad (3)$$

$$\frac{\partial v_z}{\partial t} + v_r \frac{\partial v_z}{\partial r} + \frac{v_\theta}{r} \frac{\partial v_z}{\partial \theta} + v_z \frac{\partial v_z}{\partial z} = -\frac{1}{\rho} \frac{\partial p}{\partial z} + \nu \nabla^2 v_z, \quad (4)$$

where

$$\nabla^2 = \frac{1}{r} \frac{\partial}{\partial r} \left( r \frac{\partial}{\partial r} \right) + \frac{1}{r^2} \frac{\partial^2}{\partial \theta^2} + \frac{\partial^2}{\partial z^2}.$$

The flow in an infinite rectilinear conduit with a circular section and constant diameter is a case of parallel flow. By introducing a cylindrical coordinate system with the  $z$  axis along the axis of the duct, by axial symmetry the solution has the form

$$\mathbf{V} = \{0, 0, u(r)\}$$

with the boundary condition  $u(R) = 0$ , where  $R$  is the radius of the circular section. In addition,  $p = p(z)$ .

In this case, the continuity equation (1) is automatically satisfied, as well as the components of the equation of momentum along  $r$  (2) and along  $\theta$  (3). The component along  $z$  (4) become

$$\mu \left( \frac{d^2 u}{dr^2} + \frac{1}{r} \frac{du}{dr} \right) = \frac{dp}{dz},$$

since the term on the left is a function of  $r$  while on the right the pressure gradient is only a function of  $z$ , the equality is satisfied if both terms are constant and equal, from which

$$\frac{dp}{dz} = -G \Rightarrow \mu \left( \frac{d^2 u}{dr^2} + \frac{1}{r} \frac{du}{dr} \right) = -G.$$

From the first equation we get  $p(z) = C - Gz$ , while rewriting the second in the form

$$\frac{d}{dr} \left( r \frac{du}{dr} \right) = -\frac{G}{\mu} r,$$

and by integrating it is obtained

$$\frac{du}{dr} = -\frac{G}{2\mu} r + \frac{C_1}{r} \Rightarrow u(r) = -\frac{G}{4\mu} r^2 + C_1 \ln r + C_2$$

To get a finite velocity value for  $r = 0$  you have  $C_1 = 0$ , and for the condition  $u(R) = 0$  we get  $C_2 = GR^2/(4\mu)$ , whence

$$u(r) = \frac{G}{4\mu} R^2 \left( 1 - \frac{r^2}{R^2} \right)$$

and since  $G = -dp/dz$  the Hagen-Poiseuille flow velocity profile is obtained

$$u(r) = -\frac{R^2}{4\mu} \frac{dp}{dz} \left( 1 - \frac{r^2}{R^2} \right).$$

The velocity profile is a paraboloid of revolution and since the expression of the drag coefficient  $\lambda = 64/Re$  is in excellent agreement with the experimental data, this shows that the Hagen-Poiseuille solution represents with good precision the flow in a rectilinear duct with a circular section. However, this situation is valid, for a given duct, only for not too high speeds corresponding to values of the Reynolds number lower than  $Re_{crit} = 2300$ , for which there is a laminar flow represented by the Hagen-Poiseuille solution, while for higher values there is a completely different situation characterized by a turbulent flow. [3]

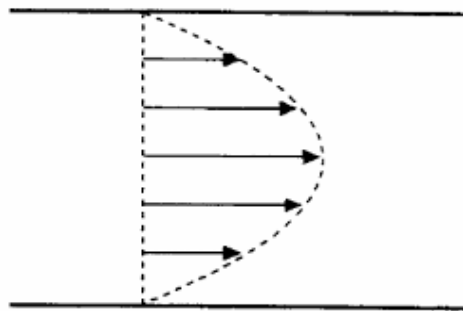
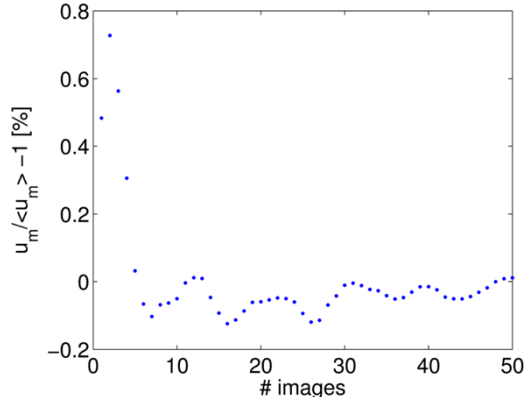


Figure 1: Simplified visualization of a Hagen-Poiseuille flow velocity profile (paraboloid of revolution).

## 1.4 TRANSITION OF PULSATILE FLOW

### 1.4.1 LAMINAR FLOW

According to Trip *et al.* [1], measurements are conducted for both steady and unsteady flow within the range of mean Reynolds number  $Re_m$  for which transition is expected ( $Re_m = 2000 - 3500$ ). The number of images  $N$  recorded is fifty, because the velocity data converged sufficiently for this number in preliminary experiments, as shown in *Figure 2*. [1]



*Figure 2*: The mean velocity  $u_m$  as function of the number of images used to average. The data are normalized using the value obtained using all available images. [1]

Before looking at the turbulence intensity, it is necessary to introduce the following equation, so that the theoretical results can be compared with the experimental results concerning the steady, oscillatory and pulsatile laminar flow velocity profiles,

$$u(r, t) = \frac{p_s}{4\mu} (r^2 - R^2) + \frac{p_o R^2}{i\mu \alpha^2} \left\{ 1 - \frac{J_0 \left( \alpha \frac{r}{R} i^{\frac{3}{2}} \right)}{J_0 \left( \alpha i^{\frac{3}{2}} \right)} \right\} e^{i\omega t}. \quad (5)$$

In this equation,  $p_s$  is the time-independent pressure gradient,  $p_o e^{i\omega t}$  the time-dependent pressure gradient, and  $\mu$  the dynamic viscosity. In the first term, the classic parabolic Poiseuille flow can be recognized, while the second term represents a flatter, phase-lagged profile representing the effects of transient inertia (note that  $J_0$  is a Bessel function of the first kind of zeroth order). [1]

Examples of instantaneous velocity profiles of typical pulsatile flow are shown in *Figure 3*.

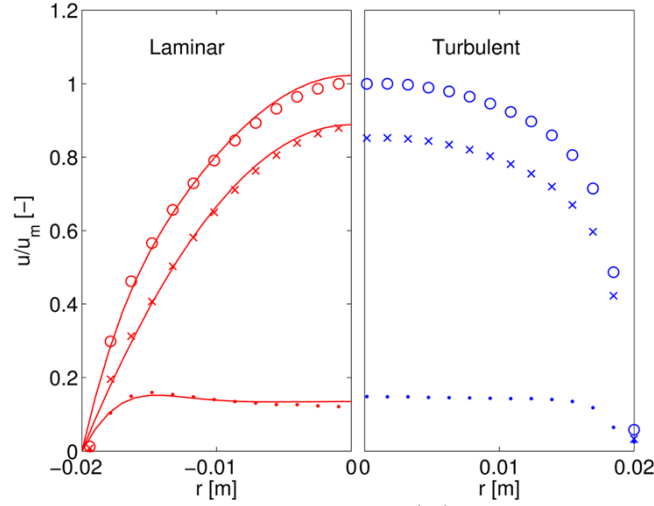


Figure 3: Left: Measured and theoretical steady  $u_s$  ( $\times$ ), oscillatory  $u_o$  ( $\cdot$ ), and pulsatile  $u_m$  ( $\circ$ ) velocity profiles of a laminar pulsatile flow ( $\alpha = 10$ ,  $Re_m = 2160$  and  $Re_o = 610$ ). Right: Measured steady  $u_s$  ( $\times$ ), oscillatory  $u_o$  ( $\cdot$ ), and pulsatile  $u_m$  ( $\circ$ ) velocity profiles of a turbulent pulsatile flow ( $\alpha = 10$ ,  $Re_m = 3160$  and  $Re_o = 610$ ). [1]

In this figure, the mean component ( $\times$ ), the oscillating component ( $\cdot$ ), and the sum ( $\circ$ , “pulsatile”) are shown for both a laminar and a turbulent case. The data has been normalized with the centerline velocity for each case. For the laminar case, the continuous lines indicate the theoretical prediction given in Eq. (5). Only the phase of the theoretical predictions has been adjusted to match the experimental data, as this particular set of data was not phase-locked. Paying attention to the turbulent case, the velocity is uniformly distributed as the presence of vortex structures allows a more functional transport of the momentum. [1]

The laminar velocity profile, on the other hand, is probably distorted due to the high Reynolds numbers that generate non-ideal inlet conditions that persist in the laminar case. [1]

#### 1.4.2 TRANSITION OF STEADY FLOW

The transition of steady flow is examined first by Trip *et al.* [1]. The turbulence intensity is measured for a mean Reynolds number from  $Re_m = 2000$  to  $Re_m = 3500$ . Because the volumetric flow rate is controlled, the mean Reynolds number is corrected for the temperature dependence of the kinematic viscosity. The turbulence intensity is the statistical average over fifty realizations.

In Figure 4, the turbulence intensity at the centerline based on the, respectively, the radial and axial velocity fluctuations are shown. Error bars denote the standard error of the mean. For the axial component, a large overshoot is shown for  $Re_m = 2388$ . [1]

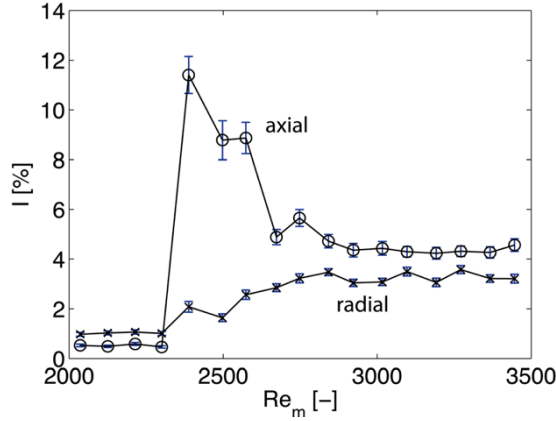


Figure 4: Turbulence intensity  $I$  at the centerline, determined by normalizing the velocity fluctuations with the centerline velocity, as function of the mean Reynolds number  $Re_m$  for steady flow. The axial  $I_a$  (○) and radial  $I_r$  (×) component of the turbulence intensity are shown separately. [1]

In accordance with what is reported in the previous paragraph, because of the more efficient momentum transfer, the mean velocity component of turbulent flows is smaller compared to laminar flow. Due to the intermittent nature within the transitional regime, the ensemble average of the mean velocity component is biased and the result for the velocity fluctuations increases as a result. For Trip *et al.* [1] the overshoot does not give a clear value for the intermittency, although might be considered physical because the turbulence intensity is a statistical quantity. One way to avoid the overshoot is by looking at the radial velocity component, for which the mean component is equal to zero for both the laminar and turbulent flow state. As a result, no overshoot is shown for radial component of the turbulent intensity as shown in Figure 4. To get a better understanding of turbulence during transitional flow, the turbulence intensity based solely on the radial component  $v'$  is more appropriate here and will be used for the remainder of this section, according to Trip *et al.* [1]

The turbulence intensity normalized by the centerline velocity is  $I_r \approx 1\%$  for a mean Reynolds number up to  $Re_m \approx 2400$ . As attested by Trip *et al.* [1], the turbulence intensity of this flow, which is still considered to be laminar, is a result of all contributions not related to turbulence like measurement errors and small fluctuations in the pump output. An increase in intensity can be observed in a range that is referred to as transitional ( $Re_m \approx 2400 - 2800$ ). Within this region, puffs occur randomly in time. For an increasing  $Re_m$ , an increasing number of puffs occurs until the flow has become turbulent at every instance which is the case for  $Re_m > 2800$ . The turbulence intensity at this Reynolds number normalized by the centerline velocity is  $I_r \approx 3\%$ . This range is consistent with the range expected based on the flow conditions and the orifice plate used. [4] The boundaries for laminar, transitional, and turbulent flow measured here will be used as a reference for the results of unsteady flow, in line with the study of Trip *et al.* [1]

### 1.4.3 TRANSITION OF UNSTEADY FLOW

A straightforward calculation of the turbulence intensity is not a satisfactory metric due to the intermittent character of the flow in the transition range. A solution is to subtract the line average in the axial direction for each fluctuating velocity field

$$\Psi'_{mod,i}(x, r) = \Psi'_i(x, r) - \frac{1}{L} \int \Psi'_i(x, r) dx . \quad (6)$$

One should notice this is only valid if the turbulent structures are large compared to the width of the field of view. As stated in the study of Wagnanski and Champagne [5], a typical puff is over 20 diameters in length and, therefore, extends over multiple measurement volumes. The error made because only part of the puff is within the field of view is small for that reason. Although the pump oscillations produce uniform variations in speed in the axial direction, the turbulent structures do not.

In the analysis of Trip *et al.* [1], the series of measurements for unsteady flow is conducted over a range of mean Reynolds numbers  $Re_m$  for a single velocity amplitude, i.e.,  $Re_o = 610$  and four Womersley numbers ( $\alpha = 10 - 25$ ) representative for blood flow within the aorta and arteries. Measurements are conducted phase-locked at eight instances during each flow cycle. The required measurement frequency and total measurement time for each case are shown in *Table I*.

*Table I*: Measurements of unsteady pulsatile flow with a Womersley number  $\alpha$ , where  $f$  is the frequency of the pulsation,  $f_t$  the frequency of measurements,  $T_t$  the total measurement time based on 50 image pairs per phase, and  $u'/D$  an estimate of the reciprocal value of the turbulence integral time-scale. [1]

$\alpha$ [-]	$f$ [1/s]	$f_t$ [1/s]	$T_t$ [s]	$u'/D$ [1/s]
0	0.0000	1.000	50	0.0775
10	0.0398	0.318	1256	0.0900
15	0.0895	0.716	559	0.0692
20	0.1592	1.273	314	0.0825
25	0.2487	1.989	201	0.0955

Based on the modified velocity fluctuation field  $\Psi'_{mod}$ , the turbulence intensity is calculated at the centerline. The turbulence intensity is normalized by the centerline velocity and averaged over time. The results are shown in *Figure 5*. [1]

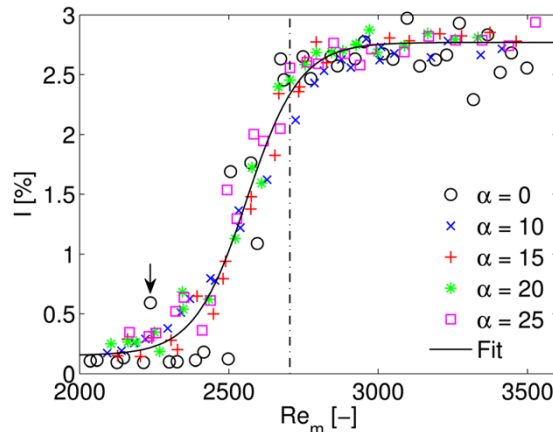


*Figure 5*: Turbulence intensity  $I$  at the centerline based on  $\Psi'_{mod}$  normalized by the centerline velocity as function of the mean Reynolds number  $Re_m$  for five different Womersley numbers. The dotted line indicates the mean Reynolds number for which the dependence on oscillatory Reynolds number is shown in *Figure 3*. The arrow marks a specific measurement discussed in the text. [1]

The results for the steady case, i.e., the result described in *Sec. 1.4.2*, are shown as open circles ( $\alpha = 0$ ). Compared to the results based on the radial velocity fluctuation component, discussed

in *Sec. 1.4.2*, the turbulence intensity at the centerline for steady laminar flow has decreased to a value of  $I \approx 0.1\%$ . This observation confirms that the new method to compute the velocity fluctuation does indeed also provide a correction for pump fluctuations. [1]

As reported in *Table I*, due to the difference in measurement frequency, a puff is captured in more instantaneous velocity fields for higher Womersley numbers. As per Kuik *et al.* [6], for the unsteady cases, the total measurement time is long compared to the survival time of a puff. As a result, the statistics average out with little influence of individual puffs. For the steady case, however, the total measurement time is short compared to the survival time. Consequently, a puff (if present) will be present in a larger fraction of the total measurement time and this means that the statistics will be more strongly influenced by the possible presence of a puff. As a result, the transition (as reported in *Figure 5*) seems to be less gradual. This hypothesis is underpinned by evaluating the data that is associated with the apparent outlier marked with an arrow in *Figure 5*, for ( $Re_m = 2237$  and  $\alpha = 0$ ). Visual inspection of the velocity fields supports the conclusion that this “outlier” is the result of a single puff. In keeping with the research of Trip *et al.* [1], this problem can be overcome by recording significantly more image pairs, but this turned out to be unfeasible in practice. [1]

To confirm the presence of puffs, the flow is visualized using Iriodin flakes. For both steady and unsteady transitional flow, a series of images is recorded with a frame rate of  $f_t = 10 \text{ Hz}$  to capture the passage of a puff. To obtain a spatial reconstruction, images are stitched together with a spatial distance based on the average velocity of the puff which is approximately equal to the bulk velocity. [1]

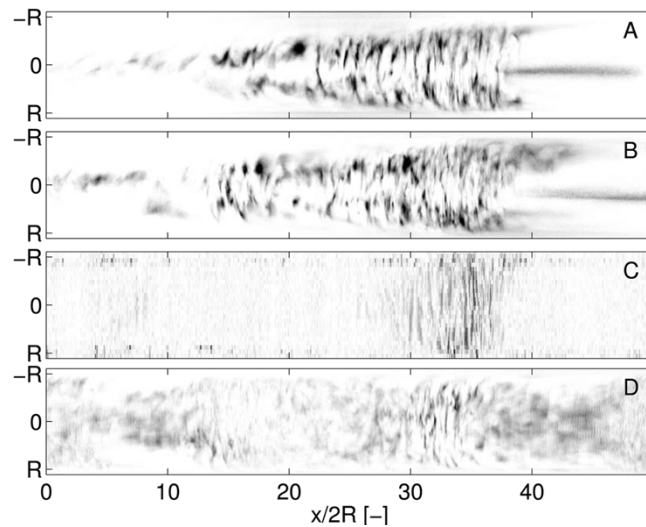


*Figure 6*: A visualization of a puff for unsteady (A) and steady (B) base flow. Image (C) gives the velocity fluctuations in the radial direction obtained by PIV. The phase-locked turbulence regime is shown in (D). The flow direction is from right to left. (Notice that the horizontal axis is compressed relative to the vertical axis). [1]

In *Figure 6*, the characteristic shape of a puff [7] is clearly recognizable for both steady as well as unsteady flow, i.e., a conical tail of turbulence at the centerline downstream side of the puff and initial turbulence at the wall at the upstream side. The figure also shows velocity fluctuations in the radial directions measured with PIV. The PIV data are combined in a similar way to the visualization images. The velocity data appears to show a much smaller puff, but this is actually caused by the large velocity fluctuations in the core of the puff compared to the fluctuations in its downstream tail. As stated by Trip *et al.* [1], a visual inspection of the data showed that the flow consisted of small, isolated turbulent structures; they also did not observe growing slug-like structures that start to appear in steady flows at Reynolds numbers above

2400-2700. A detailed comparison of the full flow structure of the puffs in the steady and pulsatile cases would be interesting, but cannot be done with the present measurement facilities. [1]

Returning to *Figure 5*, no clear differences can be observed for the different pulsatile flows. Therefore, a single fit through all values is shown in *Figure 5*. This agrees with results of Stettler and Hussain [8] who found that the influence of pulsation is limited to  $\alpha < 10$ . The s-like shape of the turbulence intensity graphs (*Figures 4 and 5*) resembles the graph of the intermittency as a function of Reynolds number as reported in Yellin [9], data which was obtained by flow visualization. This confirms our hypothesis that the increase in puff number causes the smooth increase in turbulent intensity. [1]

The question arises if the oscillatory Reynolds number influences the turbulence intensity for a fixed mean Reynolds number. For  $Re_m \approx 2700$ , the turbulence intensity is shown in *Figure 7* as a function of the oscillatory Reynolds number. [1]

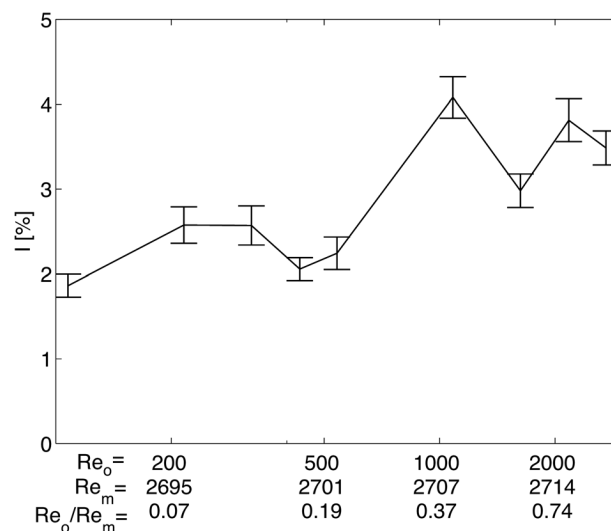


*Figure 7*: Turbulence intensity  $I$  as a function of the oscillating Reynolds number  $Re_o$ . The corresponding temperature-corrected mean Reynolds numbers  $Re_m$  and the ratio  $Re_o/Re_m$  are also indicated. [1]

At first sight, it appears that the turbulence intensity increases with  $Re_o$ . However, as the temperature was not completely constant during the measurement, the mean Reynolds number  $Re_m$  increases slightly. Therefore, the observed increase in turbulence intensity is likely explained by the increase in the mean Reynolds number, rather than due to the different oscillatory Reynolds numbers (see e.g., the slope shown in *Figure 5* for  $Re_m = 2700$ , indicated by the dashed line). Consequently, it can be concluded that the turbulence intensity is not a function of the oscillating Reynolds number; this indirectly suggests that the transition behavior is also not influenced by this parameter. *Figure 7* also shows that there is no clear relation between  $Re_o/Re_m$  and the turbulence intensity. [1]

## 1.5 PHASE-LOCKED TURBULENCE

For a Womersley number up to  $\alpha = 25$ , phase-locked turbulence is expected for mean Reynolds number  $Re_m > 2700$  and oscillatory Reynolds numbers  $Re_o > 1400$  [9]. None of the parameters  $Re_m$ ,  $Re_o$ ,  $Re_o/Re_m$ , or  $\alpha$  gives a clear boundary between the two regimes indicated here. As expressed in their study by Trip *et al.* [1], the phase-locked turbulence is a completely different phenomenon compared to the random occurrence of puffs. They assume that it is not likely that a local patch of turbulence that travels through the pipe appears phase-

locked at a fixed measurement location for every flow cycle, but a more likely explanation would be that the entire flow bursts into turbulence and then (partially) relaminarizes. [1]

Two measurements are carried out by Trip *et al.* within the phase-locked regime, for which the parameters are given in *Table II*. The PIV measurements shown are an average over 100 cycles and a 50% overlap of the interrogation areas is used to obtain a higher resolution in the radial direction, required to resolve the radial dependence of the turbulence intensity. The bulk velocity is used as the reference velocity to define the turbulence intensity. Besides the PIV measurements, a flow visualization is carried out as well. [1]

*Table II*: Measurements of unsteady pulsatile flow with Womersley number  $\alpha$ , the frequency of the pulsation  $f$ , the frequency of measurements  $f_t$  based on the number of phase-locked measurements per cycle, and  $u'/D$  an estimate of the reciprocal value of the turbulence integral time-scale. [1]

$Re_m$	$Re_o$	$Re_o / Re_m$	$\alpha$	$f$	$f_t$	$u'/D$
[-]	[-]	[-]	[-]	[1/s]	[1/s]	[1/s]
4000	1610	0.40	15	0.0895	3.580	0.1000
5000	4000	0.80	20	0.1592	3.184	0.1350

To analyze the occurrence of turbulence as a function of the phase of pulsatile flow, it is worthwhile to look at the turbulence characteristics over the pipe radius as function of phase first, as shown in *Figures 8 and 9*. [1]

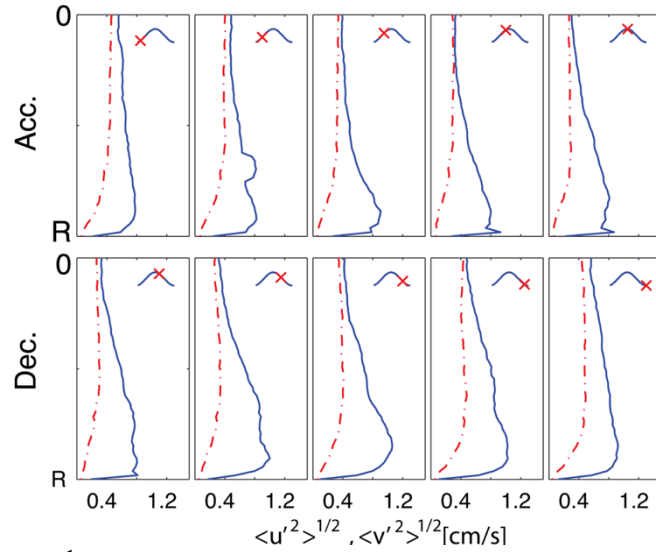


*Figure 8*:  $\langle u'^2 \rangle^{1/2}$  and  $\langle v'^2 \rangle^{1/2}$  as function of time over the radial position  $r$  with  $R$  the pipe radius for  $Re_m = 4000$ ,  $Re_o = 1610$ , and  $\alpha = 15$ . The accelerating (Acc.) and decelerating phases (Dec.) are shown at the top and bottom rows, respectively, with an indication of the phase with respect to the bulk velocity flow cycle in the insets of each sub-image. [1]

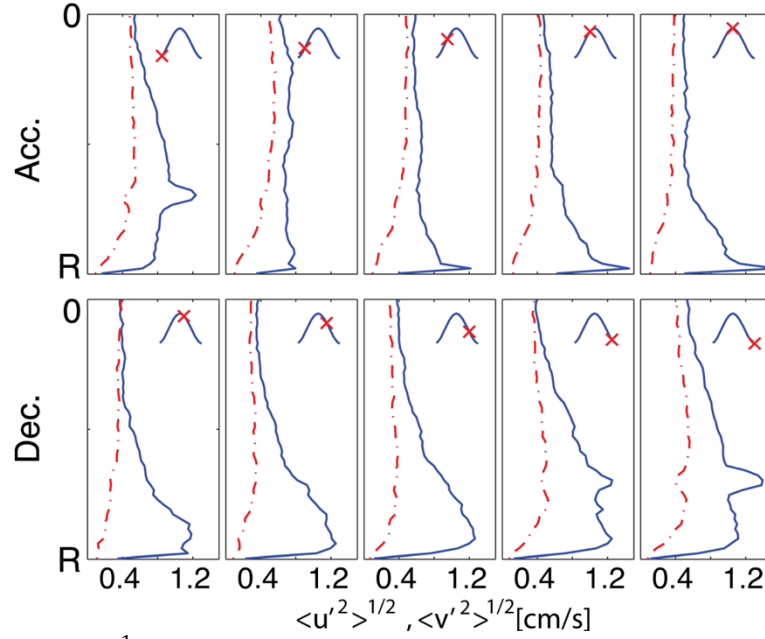


Figure 9:  $\langle u'^2 \rangle^{1/2}$  and  $\langle v'^2 \rangle^{1/2}$  as function of time over the radial position  $r$  with  $R$  the pipe radius for  $Re_m = 5000$ ,  $Re_o = 4000$ , and  $\alpha = 20$ . The accelerating (Acc.) and decelerating phases (Dec.) are shown at the top and bottom rows, respectively, with an indication of the phase with respect to the bulk velocity flow cycle in the insets of each sub-image. [1]

For several phases in both cases a small “bump” in  $\langle u'^2 \rangle^{1/2}$  and  $\langle v'^2 \rangle^{1/2}$  is shown around  $r = 3/4 R$ . These are actually artifacts caused by reflection of light in the raw PIV images that are insufficiently corrected for by image background reduction. A reflection causes the mean velocity to decrease as reflections are stationary. When the mean velocity is subtracted this leads to a higher apparent fluctuating component. [1]

To characterize the turbulent intensity in the entire pipe, the turbulence intensity is integrated over the pipe radius. Because the turbulence intensity in the azimuthal direction cannot be measured with planar PIV, it was assumed to be equal to the radial turbulence intensity because the mean velocity is zero in this direction as well. The turbulence intensity during a cycle for both  $Re_m = 4000$  and  $Re_m = 5000$  are shown in Figures 10 and 11. The turbulence intensity has here been determined by averaging the RMS value for all realizations within one phase. [1]

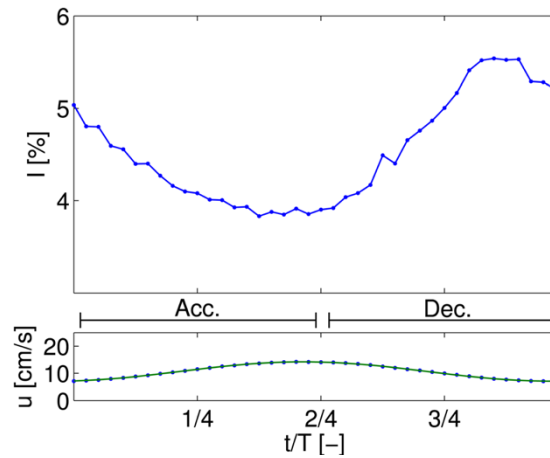


Figure 10: Turbulence intensity  $I$  as function of time  $t/T$  for  $Re_m = 4000$ ,  $Re_o = 1610$ , and  $\alpha = 15$ . The top figure shows the bulk velocity to indicate the flow cycle. [1]

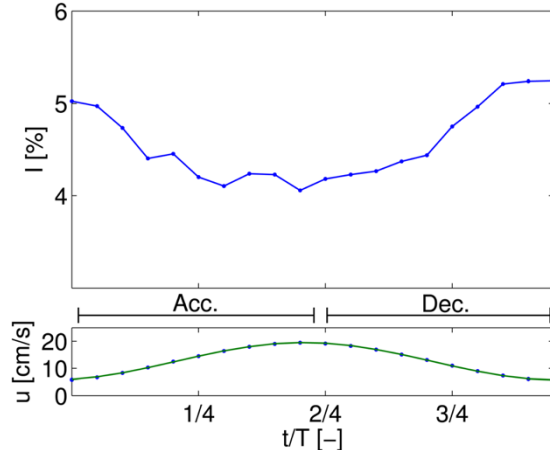


Figure 11: Turbulence intensity  $I$  as function of time  $t/T$  for  $Re_m = 5000$ ,  $Re_o = 4000$ , and  $\alpha = 20$ . The top figure shows the bulk velocity to indicate the flow cycle. [1]

Looking at the two figures above it is possible to notice that the turbulence intensity decreases during the accelerating phase and starts to increase during deceleration. Also, a maximum is reached just before the end of the deceleration phase after which it remains constant. For  $Re_m = 5000$  a decrease is shown for the remainder of the cycle. Both cases show that the turbulence intensity maintains the same phase lag relative to the velocity. This observation is in excellent agreement with results shown by Ramaprian and Tu [10], but one should notice that their results concerned the centerline fluctuations only. Akhavan *et al.* [11] report the turbulent kinetic energy integrated over the cross section, but these results are opposite to the results shown here. In fact, maximum turbulent kinetic energy was found at the end of the accelerating phase instead of at the moment of largest deceleration. A possible explanation, proposed by Trip *et al.*, is the oscillatory nature of their flow, i.e., no mean velocity component, instead of the pulsatile flow studied here. In the present case, even during the decelerating phase, the velocity always has the same sign. [1]

A plausible explanation for the relation between velocity and turbulence intensity is given by Bluestein and Einav [12]. It is mentioned that disturbances are generally observed to occur during flow deceleration. During deceleration, the flow exhibits inflection points in the velocity profiles, which is a condition that might lead to an unstable flow. As the velocity approaches a minimum, the free stream can no longer feed the turbulence and the turbulent structures that have just formed start to decay. Whether the flow will completely relaminarize during the accelerating phase probably depends on the oscillating frequency, since it takes some time for turbulence to decay. For the cases examined here by Trip *et al.*, the flow does not completely relaminarize. This can be explained by the turbulence integral time-scale, which is of the same order of magnitude as the frequency of the pulsation (see *Table II*). Simply stated, there is simply not enough time for turbulence to decay completely. [1]

Whether turbulent patches are present or the flow bursts into turbulence over, the entire pipe at once is difficult to conclude from the PIV measurements recorded for a relatively small observation window. Flow visualization using Iridin flakes was again used to observe the transition over the entire pipe length at once. Visual inspection (see e.g., *Figure 6(D)*) show that the flow does not relaminarize completely, but remains turbulent. The structures during the accelerating phase are large compared to the pipe radius. It is not possible to conclude whether the structures are located near the wall. When the minimum velocity has been nearly reached the flow abruptly burst into small structures at apparent random axial locations within the entire pipe, swiftly growing throughout the entire pipe length. [1]

## 2. EXPERIMENTS AND NUMERICAL SIMULATIONS

### 2.1 XU ET AL. EXPERIMENT N°1

These experiments were reported in *Sec. 2* of Xu *et al.* 2017. [13]

#### 2.1.1 EXPERIMENT'S SET UP

The experiments conducted by Xu *et al.* 2017 [13] were carried out in straight rigid pipes of circular cross-section and three set-ups were used which mainly differed in the pipe diameter and the pipe length.

- *Case I*: the pipe is composed of five glass tubes resulting in a total length of 5.5 m. Tubes have an inner diameter of  $D=10\pm 0.01$  mm and hence a dimensionless length of 550D. Taking the entrance length into account the remaining measurement length is 350D.
- *Case II*: the pipe was composed of acrylic tubes (inner diameter  $D = 7.18 \pm 0.02$  mm) and had a total length of 12 m, leading to a measurement length of 1300D.
- *Case III*: In the third case the pipe was composed of glass tubes (inner diameter  $D = 4 \pm 0.01$  mm) and had a total length of 10 m and a measurement length of 2250D.

The pipe is connected via a trumpet-shaped convergence section to a reservoir (see *Figure 12*). The rear end of the pipe is connected to a 1.2 m long piston (Pneumax) with a diameter of 40 mm that pulls the water through the pipe. The piston sits on a separate support and is coupled to the pipe via a short piece of semi-flexible tubing to dampen vibrations from the mechanical drive. As reported in their study, when run in steady motion the flow remains laminar up to  $Re = 9000$ . [13]

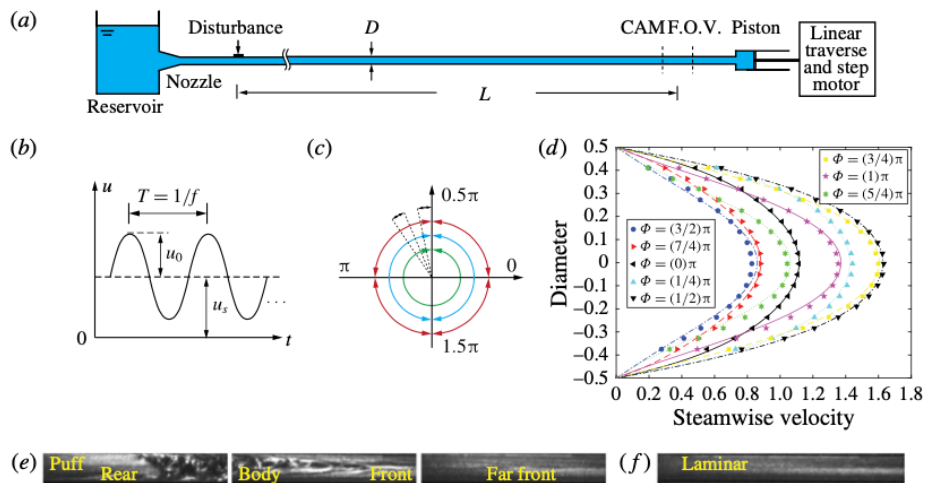


*Figure 12*: (a) Sketch of the pulsatile pipe flow set-up (pipe-1:  $D=10$  mm and  $L=350D$ , pipe-2:  $D=7.18$  mm and  $L=1300D$ , pipe-3:  $D=4$  mm and  $L=2250D$ ), (b) the sinusoidally modulated speed of the piston and (c) the phase covered by the injection perturbation. (d) Comparison of measured velocity profiles (symbols) and analytical solutions (lines in corresponding color) at  $Re_s = 2000$ ,  $\alpha = 5$  and  $A = 0.4$ . Typical flow visualization images are shown for turbulent (e) and laminar (f) flow. (The images display a pipe segment of about  $5D$  long and flow direction is from left to right). [13]

The piston speed was accurately controlled via a PC and was sinusoidally modulated giving rise to a pulsating flow ( $u(t) = U_s + U_o \cdot \sin(2\pi f \cdot t)$ ). For the entire parameter regime under investigation the pipe flow was laminar unless being disturbed.

Xu *et al.* 2017 report a particularly precise correspondence of the velocity profiles measured during the various phases with the analytical solution for a pulsatile laminar pipe flow. It is possible to generate disturbances inside the flow by using an electronically regulated valve that allows to briefly inject fluid into the flow from a 1mm hole located in the pipe wall. [13]

Comparing what has been written so far with the work of Florio and Mueller [14] and of Gerrard and Hughes [15] it can be concluded that the flow is fully developed when the perturbation is situated 150D downstream of the entrance.

According to Samanta, de Lozar and Hof [16]: “To ensure that the perturbation resulted in a single puff (the length of a puff is approximately 20D), the duration of injection is adjusted for each  $\alpha$  to cover a specific phase of the sinusoidal motion”, as demonstrated in *Figure 12*. The transition threshold is not affected in particular by variations in the injection phase.

For visualization purposes, the water was seeded with particles (fishsilver) and a light sheet, and a camera (MatrixVision BlueFox 121G) were positioned a certain distance L downstream from the perturbation point, as shown in *Figure 12*. The resulting images allow for a straightforward distinction between turbulent and laminar flows (see *Figure 12 e,f*). Following the evolution of the average grey scale level in the center of the tube or by examining the spatial fluctuations (obtained from the root mean square), the presence of puffs can be noted. Since the viscosity of the fluids may vary, it is necessary to supervise the temperature before each run using a calibrated Pt100. The flow rate was then automatically adjusted to ensure the desired value of  $Re_s$  ( $Re_s = U_s D / \nu$  with  $U_s$  steady component of the velocity). The *Case I* was conducted in a tube of 350D unlike the *Case II* and *Case III* in which tubes of 1300D and 2250D were used for measurements respectively due to the fact that for lower Womersley numbers the advection over a period occurred in tubes longer than the *Case I*, but it should be noted that the survival probabilities obtained in the three pipes weakly depend on the pipe length. In fact, in the longer pipes, puffs will only survive over the longer measurement length at somewhat higher  $Re$  where their lifetimes are larger. Although the differences are small (<10% for steady pipe flow) when compared to the modification of the transition threshold with Womersley number (> 50%), the threshold estimates obtained in the longer pipes converge to the actual critical point where the turbulence eventually becomes sustained. [13]

## 2.1.2 RESULTS

Considering a certain range of some parameters such as Womersley numbers  $1.5 \leq \alpha \leq 22$ , amplitudes  $0 \leq A \leq 0.7$  and Reynolds numbers  $Re_s < 3500$ , it was possible to evaluate the reaction of the transition to the effect of pulsation. As shown in *Figure 13a*, for the considered parameters the flows appear as laminar as long as they are not disturbed, thus resulting in the laminar flow as linearly stable. Nevertheless, the sight of localized patches of turbulence can be traced back to perturbations generated for large enough  $Re_s$  (shown in *Figure 13b*). [13]

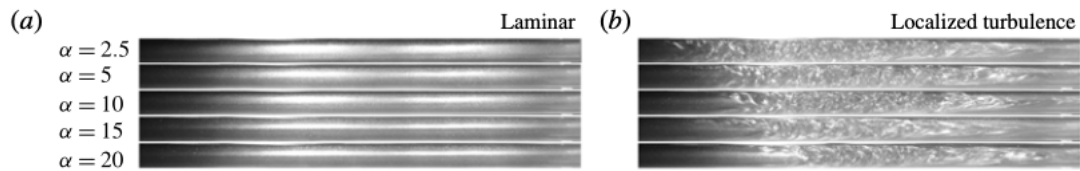


*Figure 13:* Visualization samples of laminar flow which is observed in the absence of external perturbations (a). When perturbed upstream, turbulence could be excited locally (b). The examples shown are for parameter values of  $(\alpha, Re_s)$  of  $(2.5, 3100)$ ,  $(5, 2800)$ ,  $(10, 2500)$ ,  $(15, 2500)$ ,  $(20, 2500)$  from top to bottom. The flow direction is from left to right. [13]

For fixed combinations of  $(\alpha, A)$ ,  $Re_s$  was varied to find the regime where sufficiently strong perturbations first result in turbulent puffs. Subsequently, remembering that the measurement distance is 350D for pipe 1, 1300D for pipe 2 and 2250D for pipe 3, it was possible to identify the probability, as a function of  $Re_s$ , that the puffs existed over a fixed distance. [13]

Previously reported values (black solid curve in *Figure 14*) by Hof *et al.* 2008 [17] still agree with the case of a steady flow rate (red circles in *Figure 14a*) despite having moved from operating with pipes operated at a constant pressure head to estimating the probabilities of survival with piston driven set-up (pipe 1) respectively. According to Hof *et al.* 2006 [18], 2008 [17], a S-shaped curve represents the survival probability which is an increasing function with  $Re$  until it reaches a higher asymptotic plateau where the survival probability  $P = 1$  is approximated asymptotically and this also suggests the transient nature of individual puffs. Consequently to the transient nature of the individual puffs, the survival possibilities in pulsating flow also respect the S-shaped curves as represented in *Figure 14*, for a fixed pulsation amplitude of  $A = 0.4$ , to estimate the effect of pulsation frequency. For small Womersley numbers S curves are considerably shifted to the right and hence much higher  $Re_s$  are required to observe puffs of appreciable lifetimes. For large Womersley numbers on the other hand puff survival probabilities approach the steady pipe flow case and the transition point appears to be unaffected by flow pulsation. [13]

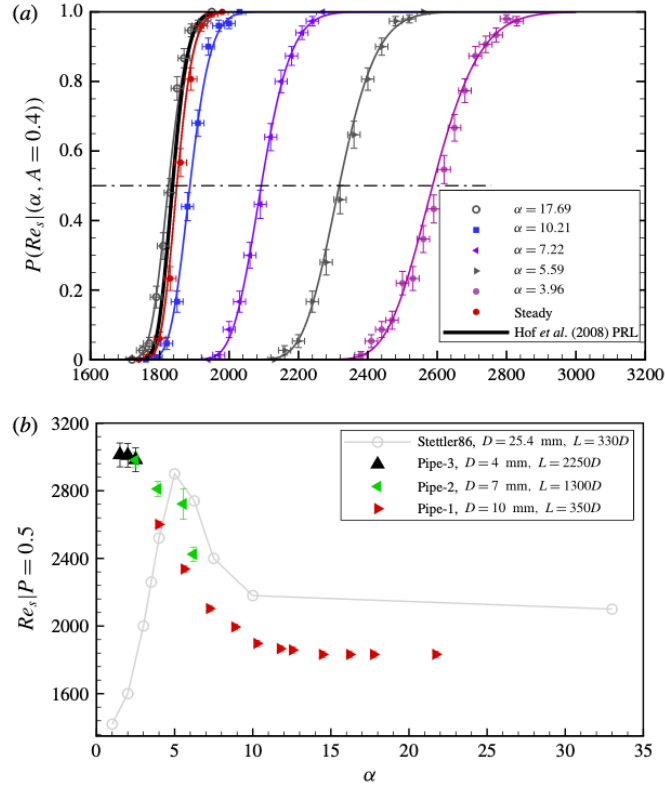


Figure 14: (a) The survival probability of individual puffs, measured 350D downstream from the perturbation point. Plotted are the survival probabilities as a function of  $Re_s$  for various pulsation frequencies and a fixed amplitude of  $A = 0.4$ . The corresponding lines indicate super-exponential fits to the respective data sets. The black curve shows the lifetime scaling for steady pipe flow from Hof *et al.* 2008 [17]. For clarity not all measured data sets are plotted. The dash-dot line marks  $P = 0.5$ . (b) The Reynolds number for which  $P = 0.5$  is plotted as a function of Womersley number. Measurements are carried out for three different lengths, corresponding to three different observation times  $t = 350, 1300$  and  $2250$  (for all cases puff advection speeds are close to 1). Subtracting the puff formation time  $t_0 \approx 100D/U_s$  the obtained Reynolds number values then map out the thresholds where puff lifetimes reach 250, 1200 and 2150 advective time units respectively. The results of Stettler and Hussain [8] are shown in grey for comparison. [13]

As shown in Figure 14b for  $\alpha > 12$  50 % survival probabilities are reached at the same Reynolds number as in steady flow ( $Re \approx 1860$  for  $L = 350D$ ). For  $\alpha < 12$  however transition is delayed and significantly higher Reynolds numbers ( $Re_s = 2960$  for  $\alpha = 2.5$ ) are necessary to obtain puffs of the same lifetimes as in the steady case. Measurements of puff lifetimes at lower Womersley numbers had to be carried out in the longer pipe set-ups, in order to ensure that puffs experience a full oscillation cycle before they exit the pipe. The data sets (Figure 14b) taken in the two longer pipes show the same general trend, transition thresholds keep increasing with decreasing Womersley number. As stated by Xu *et al.* 2017 “In contrast to earlier studies of this parameter regime that reported transition to occur earlier than in steady flow, the transition threshold continues to increase and there is no sign of a reversal of this trend. The rate of increase however slows down for  $\alpha < 2.5$ .” [13]

It is necessary to underline that in this experiment the impact on the transition of the pulsation amplitude as well as of the Womersley number was examined by fixing the pulsation frequency while  $A$  was varied. Considering the S-shaped curves shown in Figure 15 it was possible to determine  $Re_s | P = 0.5$  and puff survival probabilities have once again been established. [13]

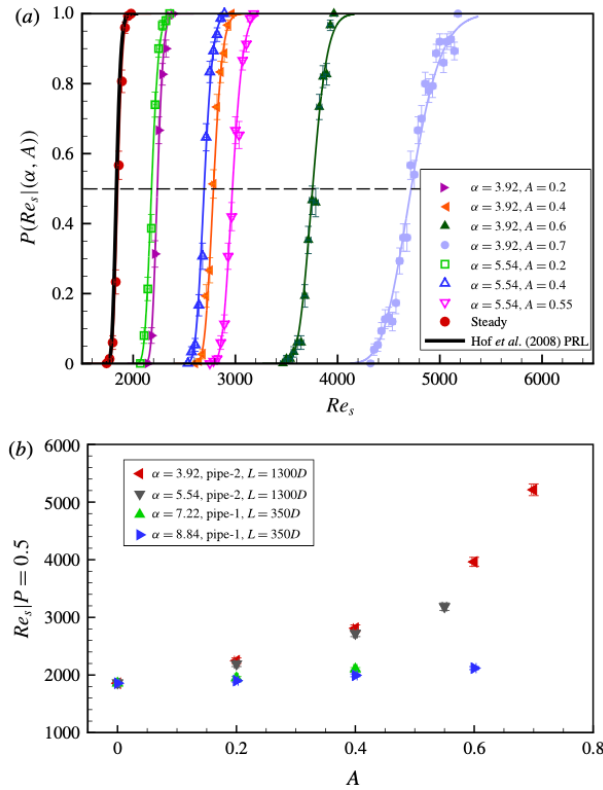


Figure 15: (a) The survival probability of individual puffs measured for varying pulsation amplitudes. The dashed line marks  $P = 0.5$ . (b) The Reynolds number threshold values (50% survival probabilities) are plotted as a function of the pulsation amplitude. [13]

As shown in Figure 15a the characteristic S shapes are shifted considerably to higher  $Re_s$  and the transition delay increases with pulsation amplitude. When the pulsation amplitude increases, the  $Re_s | P = 0.5$  increases monotonically and this was found for all four frequencies considered (Figure 15b) and this transition delay is most prominent for low frequencies while at large frequencies the increase with amplitude is only moderate. [13]

### 2.1.3 DISCUSSION

Due to the number of control parameters it is difficult to evaluate the transition process in linearly stable flows. As stated by Xu *et al.* 2017 “Puffs are the first turbulent structures to arise in the subcritical regime of pulsatile pipe flow, and lifetimes of turbulent puffs provide a natural and very accurate measure of the transition threshold, because small changes in the governing parameters can change mean lifetimes by several orders of magnitude”. [13]

If perturbation levels to trigger turbulence depend on  $\alpha$  or if the noise levels present in the experiments change with  $\alpha$ , experiments lacking an active triggering mechanism become very difficult to interpret.

By comparing this work with previous work by Stettler and Hussain [8] and Trip *et al.* [1], underlining that in all three studies turbulence was actively triggered, it can be observed that the transition threshold does not change in the large frequency limit ( $\alpha > 12$ ) while puff lifetimes is significantly reduced if Womersley number decreases below 10 so that consequently also the transition is delayed to larger  $Re_s$ . Dwelling in comparison with the work of Stettler and Hussain [8], in which the length of the tube used was inadequate for examining such low Womersley numbers, they noted a transition delay for  $5 < \alpha < 10$  and differently from the experiment of Xu *et al.* [13] recorded a decrease of the transition threshold for  $\alpha < 5$ .

There was a monotonous increase in the transition delay with the variation of the pulsation amplitudes and it is particularly marked at low  $\alpha$ . Taking up the study by Stettler and Hussain [8], they too reported a transition delay in this regime but for larger amplitudes the transition recoiled towards lower Reynolds number. [13]

By monitoring the process of growth and decay of turbulence by means of the simplified case of a square-wave pulsation, in which the Reynolds number jumps between two defined levels, it is possible to notice the upward shift of the transition point. At  $Re = 2856$ , i.e. the faster half, the flow was altered with a puff that was simulated at  $Re = 2040$  in the same pipe. Then the puff starts to grow turning into a slug. At the jump to the lower cycle at  $Re = 1224$ , the mass flux was considerably changed (mean flow speed) while keep the turbulent fluctuations unchanged, in such a way that this imitates the situation in experiment in which the mass flux is changed quickly by, e.g. abruptly adjusting the speed of the driving piston. An oscillation period of 120 advective time units (corresponding to a Womersley number of 5) was simulated. [13]

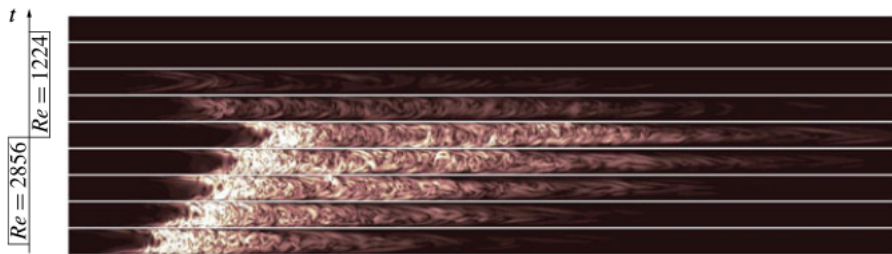


*Figure 16:* Direct numerical simulation of a puff in a square-wave motion at  $Re_s = 2040$  with  $A = 0.4$ . From bottom to top, each snapshot shows the contour of the streamwise vorticity normalized by mean velocity of  $Re_s$ , from  $t = 0$  to  $t = T$  with an equal time interval of  $T/8$ . [13]

As shown in *Figure 16* during the faster half of the square-wave cycle ( $Re = 2856$ , bottom half of *Figure 16*) turbulence rapidly expands. After half of the oscillation period (60-time units)  $Re$  changes to 1224, and turbulence abruptly decays (top half of *Figure 16*). A key difference is that in the faster part of the cycle the turbulent patch expands outwards from its interfaces, whereas at low  $Re$  turbulence collapses throughout (rather than receding from its interfaces). As reported by Xu *et al.* 2017 [13] “The decay is much faster and clearly dominates over the growth process when viewed over one full pulsation period. This imbalance between the decay and growth implies that in the low Womersley number regime turbulence can only become sustained at significantly larger  $Re$  than in steady pipe flow, in qualitative agreement with the experimental observations.”

Considering a more regular decrease of the Reynolds number in the case of a sinusoidal pulsation, it will be noted that the collapse of the turbulence occurs less suddenly, although a small Womersley number will control the previous growth, and it will be expected that the expanding turbulent structures (i.e. slugs) collapse to puffs for quite slow decreases in the Reynolds number (up to the puff regime). To investigate if at sufficiently low Womersley numbers this proposed structural adjustment of turbulence indeed occurs flows were compared at  $\alpha = 8, 5$  and 3. In all three runs the mean Reynolds number is equal to 3000 while the pulsation amplitude is 0.4. In each case the laminar flow is perturbed at  $t = T/4$  where the flow speed is at its maximum ( $Re = 4200$ ). The evolving turbulent flow was later followed downstream, and the flow field was visualized at  $t = 3T/4$ , i.e. at the minimum flow speed ( $Re = 1800$ ). [13]

At  $\alpha = 8$  turbulence takes the form of a slug-like structure (*Figure 17a*), whereas in a steady flow at the same Reynolds number (1800) slugs are unstable and only much shorter puffs can be found (see *Figure 17d*).

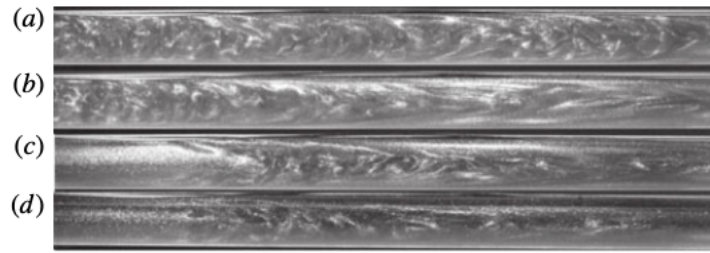


*Figure 17*: Flow structures recorded at an instantaneous Reynolds number  $Re(t) = 1800$  for various  $\alpha$ : (a)  $\alpha = 8$ , (b)  $\alpha = 5$ , (c)  $\alpha = 3$ ; (d) steady pipe flow at  $Re = 1800$ . For the pulsating flows (a–c) all other parameters are identical  $Re_s = 3000$  and  $A = 0.4$  and the images were recorded at the minimum of the cycle (i.e. at  $Re = 1800$ ). At  $\alpha = 8$  turbulence forms an elongated slug, despite the low instantaneous Reynolds number (1800). For  $\alpha = 3$  on the other hand the observed flow structure is a puff in close correspondence to puffs in steady flow of the same  $Re$  (d). [13]

The Reynolds number change appears to be too fast for turbulence to adapt to the structure characteristic for the instantaneous speed. While puffs are prone to decay, slugs are stable and hence turbulence at  $Wo = 8$ ,  $Re_s = 3000$  is sustained and well above the transition threshold. At the intermediate Womersley number (*Figure 17b*) the slug observed at the minimum of the cycle (i.e.  $Re = 1800$ ) is shorter than at  $\alpha = 8$  but still larger than the structures would be under steady flow conditions at this instantaneous  $Re$ . Finally, for  $\alpha = 3$  at the cycle minimum turbulence has reduced to a puff (*Figure 17c*), structurally equivalent to puffs in steady pipe flow at this Reynolds number (*Figure 17d*). Although during the faster part of the cycle turbulence had spread considerably (not shown) once  $Re$  drops sufficiently (here shown for  $Re = 1800$ ), the extended slug (in this example  $>100D$  at its maximum length) collapses and in this case only a single puff (at the position of the slug’s trailing edge) remained. As said by Xu *et al.* 2017 “It hence appears that at low Womersley numbers where Reynolds number changes are much slower, turbulent structures can more readily adapt to the instantaneous Reynolds numbers. As Womersley numbers further decrease one may expect that eventually turbulent structures follow the very slow changes of Reynolds number in a quasi-steady fashion. In this case the survival of turbulence would be decided over the low Reynolds number phase where turbulence consists of distinct puffs with finite lifetimes. In this limit it should then be possible to estimate the transition threshold based on puff lifetimes by integrating over the corresponding steady flow values for the corresponding Reynolds numbers.” [13]

In order to retain the same survival probability (i.e.  $P = 0.5$ ) at lower  $\alpha$  the mean Reynolds number has to go up. Therefore, the quasi-steady assumption predicts monotonically increasing threshold values  $Re_s|P = 0.5$  for decreasing  $\alpha$ . To test the quantitative agreement the results of the quasi-steady analysis are shown for comparison in *Figure 18* (dashed curve). [13]

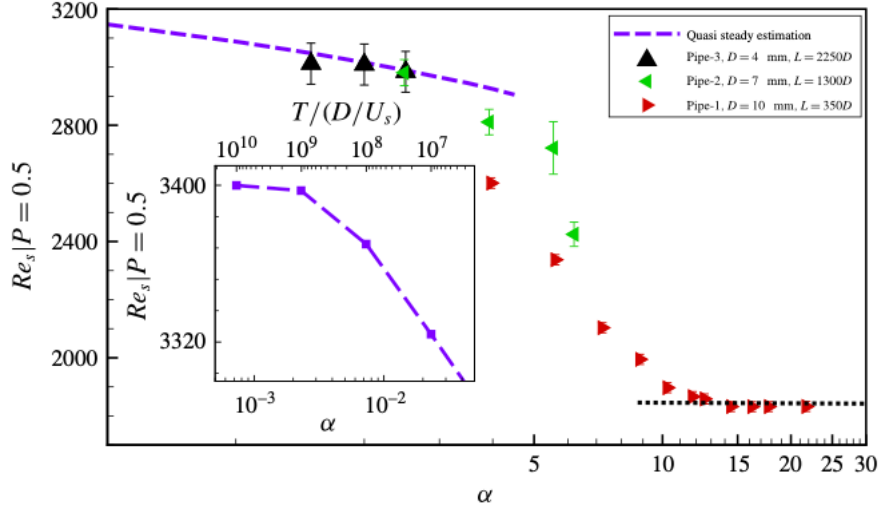


Figure 18: Estimates of the transition threshold, obtained by determining the Reynolds number value where puffs have a 50% survival probability (i.e.  $Re_s(\alpha)|P = 0.5$ ) over the respective pipe length  $L$  of the three different pipe set-ups. For comparison the (purple) dashed curve shows the 50% survival probability over a single period obtained from the quasi-steady assumption. For  $\alpha \rightarrow 0$  the curve asymptotes towards an upper bound ( $Re_s = 3400$  for  $A = 0.4$ ) (see inset). The black dotted line marks the 50 % survival probability for  $L = 350D$  (same as red circles) for steady pipe flow. [13]

For  $\alpha < 2.5$  they indeed closely capture the values measured in the pulsating flow experiment. It would appear that for the long period times (and hence the slow Reynolds number variations at these low Womersley numbers) flows indeed can be considered as quasi steady. Unfortunately, due to the very long periods at these low Womersley numbers an experimental verification of this predicted asymptotic value is not possible.

## 2.2 XU ET AL. EXPERIMENT N°2

These experiments were reported in Xu *et al.* 2020. [19]

### 2.2.1 PUFF TURBULENCE

The experiments conducted by Xu *et al.* 2020 [19] were carried out in a rigid straight pipe with an inner diameter of 7 mm and a total length of 12 m. The fluid was pulled through the pipe by a piston (Figure 19).

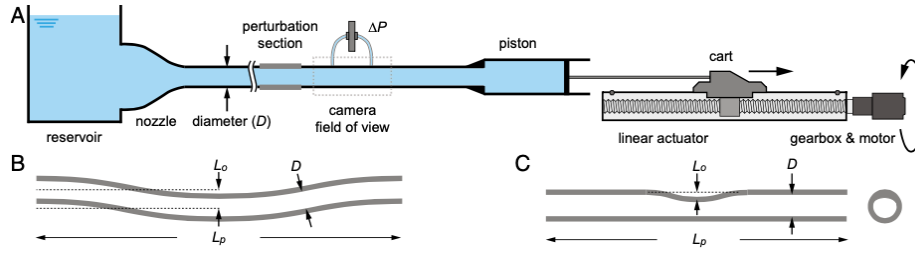


Figure 19: (A) Sketch of the pulsatile pipe flow setup. The dashed rectangle marks the measurement location where pressure and visualization measurements were carried out. The flow is from left to right. The perturbation methods are sketched in B and C, where  $D$  is the pipe inner diameter,  $L_p$  the length of perturbation section, and  $L_o$  the offset: (B) curved segment perturbation, where  $L_p = 7D$  and the offset ranges from  $0D$  (natural transition) to  $0.45D$ ; (C) constriction perturbation (mimicking unevenness), where  $L_p = 5.6D$  and the offset ranges from  $0.14D$  to  $0.7D$ . C, Right shows the cross-sectional view. [19]

The piston speed was sinusoidally modulated, imposing a cross-sectionally averaged flow velocity  $U(t) = U_m + U_o \cdot \sin(2\pi ft)$ , where  $U_m$  is the mean flow speed,  $U_o$  the oscillation component of the flow speed,  $f$  the frequency, and  $t$  the time. As suggested by the linear stability theory, the unperturbed flow remains laminar over the entire parameter regime investigated. A small hole in the pipe wall, located  $150D$  downstream of the pipe inlet, could be used to inject an impulsive jet of fluid in order to determine the susceptibility of the fluid to finite-amplitude perturbations. To visualize the flow structure, the water was seeded with reflective particles (fish silver) and a light sheet was used to illuminate the mid-cross-section (radial-streamwise) of the pipe. A turbulent puff, which is then advected downstream, has developed from the perturbed flow when the Reynolds number reaches relatively high values. An example of a puff with its characteristic intense upstream interface and a gradual downstream interface is shown in Figure 20. [19]

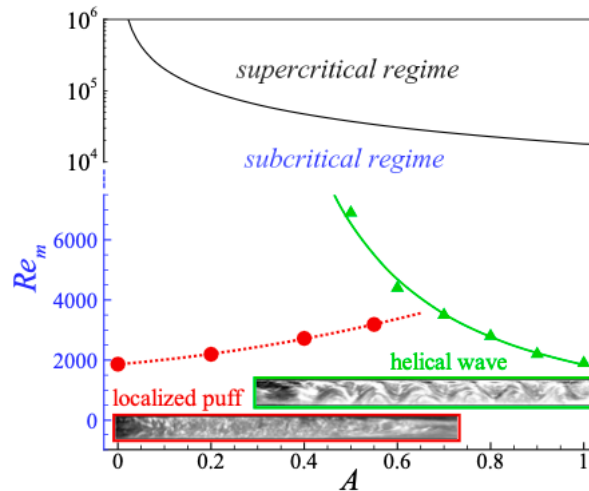


Figure 20: The threshold for the onset of puffs is given by the red dotted line. That for the onset of the helical wave instability is given by the green solid line. The Womersley number is held fixed at  $Wo = 5.6$ . The upper part (note the scale is altered to be logarithmic) shows the linear instability threshold (black curve) which sets in only at  $Re_m$  much larger than those discussed in this study. Insets show flow visualization images at  $t/T \approx 0.68$ : *Top Inset* shows the helical wave pattern and *Bottom Inset* shows a puff. The flow in both cases is from left to right. [19]

It is important to underline that just like in steady pipe flow, puffs also have finite lifetimes in pulsatile flow. It was necessary to measure the puff survival rate for varying pulsation

amplitude in order to estimate the effect of flow pulsation on the puff transition threshold. While the frequency was held constant throughout (i.e., Womersley number,  $Wo = 5.6$ ) for each selected pulsation amplitude, the Reynolds number was increased until puffs were first detected. Womersley number, pulsation amplitude, and Reynolds number are defined as follows:  $Wo = 0.5D\sqrt{2\pi f/\nu}$ ,  $A = U_o/U_m$ , and  $Re_m = U_mD/\nu$ , where  $D$  is the pipe diameter, and  $\nu$  is kinematic viscosity of the fluid. The Reynolds number where 50% of puffs survive has been evaluated as a measure of the transition threshold since for low  $Re$  all puffs decayed before the end of the pipe while for  $Re$  sufficiently large all puffs survive. For each pair of parameters ( $A$  and  $Re_m$ ) lifetime statistics were based on a sample of 150 puffs. As shown in *Figure 20* the dependence of this chosen puff survival threshold is plotted as a function of the pulsation amplitude. With increasing amplitude, the puff transition (red curve) is delayed in accordance with the previous experiments of Xu *et al.* 2017 [13].

## 2.2.2 HELICAL INSTABILITY

When the pulsation amplitude surpasses 0.7, the above trend stops, and the transition threshold begins to move to lower  $Re_m$ . Inspection of the flow structure shows that here instead of puffs a regular, helical vortex pattern is observed (*Figure 20*). Unlike puffs this structure does not result from the injection of a jet at the perturbation location, but instead it was discovered by Xu *et al.* 2020 [19] that it develops at a fixed pipe location at each cycle during flow deceleration (i.e., for  $0.6 \lesssim t/T \lesssim 0.75$  with period  $T$ ) and it decays during acceleration. Upon a further increase in the pulsation amplitude the instability threshold moves to smaller  $Re_m$ . By increasing the Reynolds number, the helical instability occurred spontaneously in order to continue the instability branch to lower amplitudes ( $A < 0.7$ ), without triggering puffs.

From the inspection of the pipe it was found that the helical (wave) instability was generated in the segment directly upstream of the pipe in which there was an axial misalignment of the order of 1 mm. When realigning the pipe, the helical instability could be postponed to larger  $Re_m$ , while further misalignment moved the instability threshold to lower  $Re_m$ . Comparing them at the same parameter values ( $Re_m, Wo, A$ ) = (2200, 5.6, 0.85), it was possible to describe the structural and dynamic differences between puffs and the helical instability: in fact, in one case the pipe segment was carefully aligned and a puff was triggered using the upstream injection perturbation while in the other case no puff was injected and the flow was perturbed by the upstream bent pipe segment. Both instances are shown for the flow deceleration phase in *Figure 21*: the puff begins to spread in the downstream direction, while its upstream interface remains at the same location; over the same part of the cycle, the helical instability gradually increases in amplitude and spreads down- as well as upstream. According to Xu *et al.* 2020 [19] “The upstream propagation indicates that the instability is of absolute nature during part of the cycle, while the puff instability for the same parameters remains convective.”

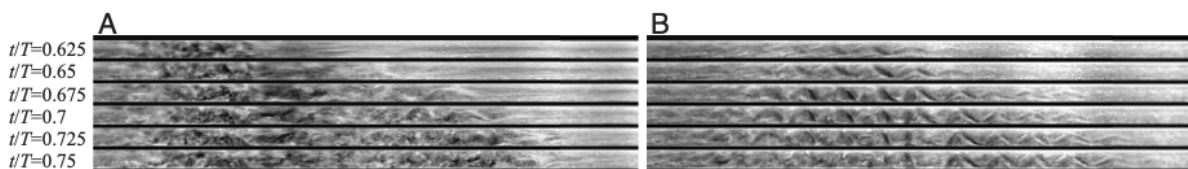


*Figure 21*: Visualization of transition to turbulence in pulsatile pipe flow in a space–time diagram at  $(Re_m, Wo, A) = (2200, 5.6, 0.85)$ . (A) The evolution of a puff which grows in the streamwise direction while its upstream interface is approximately stationary. (B) Evolution of the helical instability. The helical wave spreads downstream as well as upstream. The flow in A and B is from left to right. [19]

Making a parallelism with the cardiovascular context, it is necessary to point out that all blood vessels present deviations from the idealized straight pipe case of the same order or larger than in the previously mentioned case in which the misalignment regarded only part of a pipe diameter. By inserting a short pipe segment with a chosen moderate curvature (sketched in *Figure 19B*), while keeping the rest of the pipe straight and well aligned, it was possible to trigger the helical instability in a more controlled manner. With a more strongly curved pipe segment, the instability occurs at considerably lower  $Re_m$  (see green curves in *Figure 22*) and again the transition threshold decreases with  $A$ . These findings suggest that the helical instability, just like the instability to turbulence in steady flow, results from a perturbation of finite amplitude.

As reported by Xu *et al.* 2020 [19] “While the transition in steady pipe flow is characterized by a double threshold, i.e., both the amplitude of the perturbation and the Reynolds number have to be large enough, the helical instability has a triple threshold. Here in addition to the perturbation amplitude and the Reynolds number also the pulsation amplitude has to be sufficiently large. Moreover, the types of disturbance that trigger the helical instability differ from those triggering puffs.”

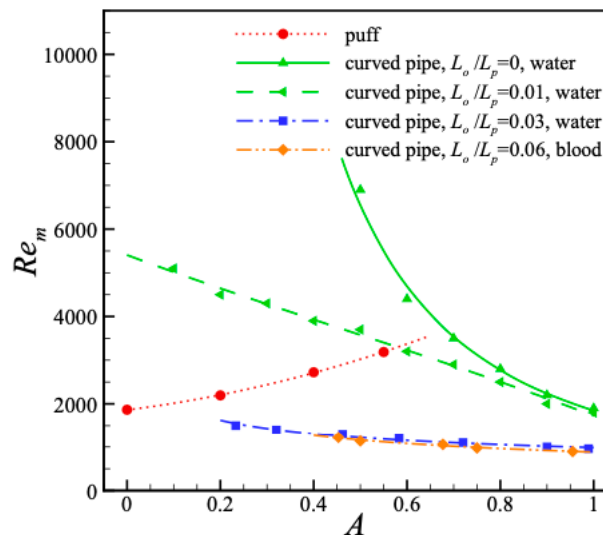


*Figure 22*: Onset of instability as a function of the pulsation amplitude for water (Newtonian) and blood (non-Newtonian). The pulsation frequencies (i.e., Womersley numbers) for the different datasets are as follows: red circles,  $Wo = 5.6$ ; green triangles,  $Wo = 5.6$ ; and blue squares,  $Wo = 5.9$ . For the blood flow measurement (orange diamonds)  $Wo = 4.0$ . [19]

### 2.2.3 HELICAL INSTABILITY IN SIMULATION

Using the Navier-Stokes equations in a numerical simulation it was possible to create a model to illustrate the origin of the instability. Although the flow is linearly stable over the considered parameter range and despite the perturbations decay considerably during the entire cycle duration, the perturbation growth can occur in a part of the pulsation cycle. A linear nonmodal transient growth analysis with an adjoint-based method was performed to determine the optimal perturbations of pulsating pipe flow. [19]

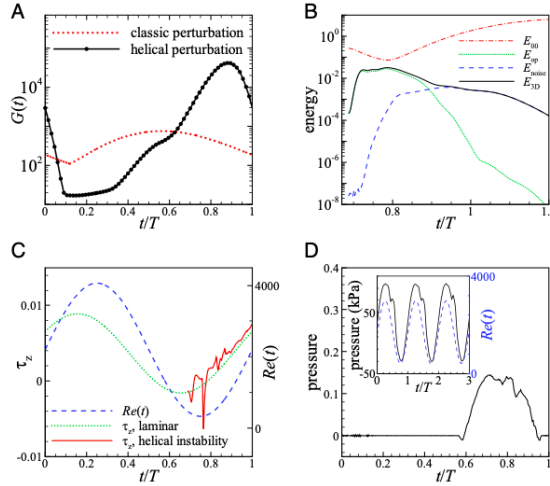


**Figure 23:** (A) Optimal linear energy growth  $G(t)$  of disturbances at  $(Re_m, Wo, A) = (2200, 5.6, 0.85)$  for the classic perturbation (streamwise independent, dotted line) and helical perturbation (solid line). (B) Direct numerical simulation of transition in a pipe of  $12D$  length disturbed with the optimal helical perturbation (for  $1.5D$  wavelength) and superposed three-dimensional (3D) noise. Shown are time series of the kinetic energy of the spatially averaged flow profile ( $E_{00}$ ) and the 3D component of the disturbance ( $E_{3D}$ ), i.e., of those Fourier modes with  $k \neq 0$  and  $m \neq 0$ . The latter is further decomposed to the part corresponding to the optimal helical perturbation ( $E_{op}$ ) and the rest ( $E_{noise}$ ). (C) Time series of fluid wall shear stress  $\tau_z$  exerting on the pipe wall at a fixed location, together with the instantaneous Reynolds number  $Re(t)$ , in the direct numerical simulation at  $(Re_m, Wo, A) = (2200, 5.6, 0.85)$ . (D) The relative deviation in pressure from the corresponding laminar case for blood flow at  $(Re_m, Wo, A) = (1140, 4.0, 0.5)$ . Inset shows the time series of streamwise differential pressure (black solid line) together with the instantaneous Reynolds number (blue dashed line) at  $(Re_m, Wo, A) = (1700, 5.9, 0.58)$ . The instability causes the smaller secondary peak in the pressure signal during flow deceleration. [19]

As shown in *Figure 23A*, the energy of infinitesimal perturbations can be amplified by more than four orders of magnitude during part of the cycle. According to the study of *Xu et al. 2020* [19] the optimal perturbation has a helical shape and yields its maximum energy amplification toward the end of the deceleration phase. In fact, this helical perturbation dominates during the deceleration phase, and the streamwise independence of the classic optimal perturbation of steady pipe flow is also relevant to pulsatile pipe flow and dominates in the acceleration phase, but features much lower amplification factors than the helical perturbation in the deceleration phase.

Subsequently, direct numerical simulations, initialized with a helical suboptimal perturbation of wavelength  $1.5D$ , were developed to be able to compare the experiments performed. After the initial development and amplification of the helical wave, breakdown to turbulence occurred. The peak in turbulent kinetic energy was reached at  $t/T \approx 0.75$ , as shown in *Figure 23B*, in close agreement with experiments. The strong fluctuations and abrupt changes in shear stress that occur during this period are shown in *Figure 23C*. Similarly to the experiments, the fluctuations decayed during the acceleration phase and the flow returned to laminar and then the helical vortex pattern in the radial–azimuthal plane and the waviness in the radial–streamwise cross-section resemble those in experiments, as shown in *Figure 24*. [19]

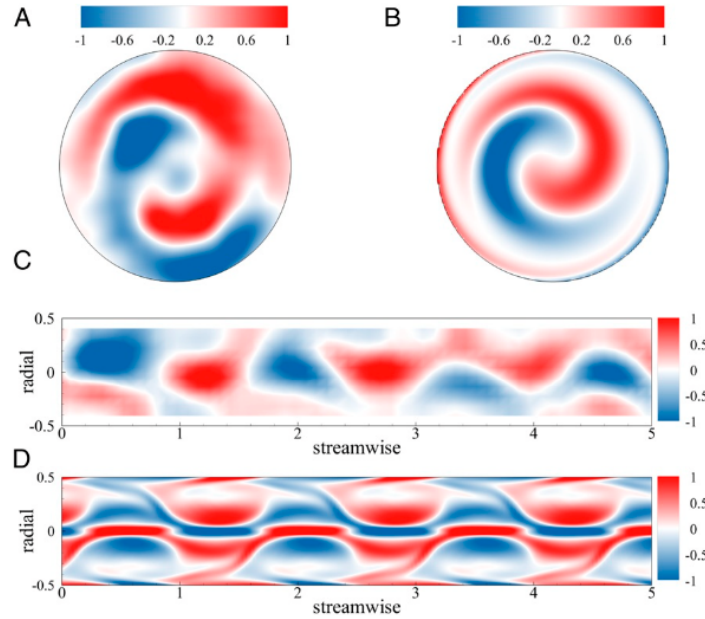


*Figure 24:* (A and B) Colormap of the streamwise vorticity in a radial–azimuthal cross-section of the pipe from experiments (A) and numerical simulations (B). (C and D) The colormap of the spanwise vorticity in a radial–streamwise plane from experiments (C) and numerical simulations (D). In both cases, a pipe segment of  $5D$  is shown. The experiment and the direct numerical simulation were both carried out at  $(Re_m, Wo, A) = (2200, 5.6, 0.85)$ , and the snapshots were taken at  $t/T \approx 0.7$ . [19]

Thus, it can be seen that a generic mechanism for the generation of helical vortices and a subsequent breakdown into turbulence is offered by the large transient amplification of disturbances during flow deceleration. [19]

From the analysis of Xu *et al.* 2020 [19], this nonmodal transient growth analysis shows that the energy of all axisymmetric perturbations decays nearly monotonically. Furthermore, the helical instability revealed here occurs at moderate amplitudes and is rooted in the strong nonmodal transient growth of helical (3D) perturbations.

#### 2.2.4 LUMEN CONSTRICTION

The replacement of the curved pipe segment by a straight section that includes a local constriction in the form of a spherical cap (up to  $D/4$  in height and a base cap diameter of  $2D$ ; *Figure 19C*) allowed to analyze whether the helical instability can occur if the cross-sections of blood vessels deviate from the idealized circular case as in the presence of protrusions due to wound healing or stenosis formation. As the Reynolds number increases at  $(Wo, A) = (5, 0.85)$ , a helical vortex pattern was found during the flow deceleration, according to Xu *et al.* 2020 [19]. In fact, the helical wave was first observed  $40D$  downstream of the protrusion and, at its maximum amplitude, the turbulent patch stretches approximately from  $35D$  to  $55D$  downstream from the spherical cap. On the other hand, the helical instability did not manifest itself in case the experiment is conducted with a slight axisymmetric constriction.

By performing experiments in the 20-mm pipe with flow parameters  $(Re_m, Wo, A) = (1100, 10, 0.8)$ , the waveform typically observed in the aorta has replaced the idealized sinusoidal flow rate in order to examine the robustness of the helical instability. As concluded by Xu *et al.* 2020 [19], it is again verified the situation where the helical instability was observed during flow deceleration followed by relaminarization as the flow was accelerated.

### 2.2.5 BLOOD FLOW EXPERIMENTS

In order to conduct experiments with blood as a working fluid, which unlike water is a non-Newtonian fluid (blood is a dense suspension of blood cells), it was necessary to use a 4 mm diameter pipe to operate in similarity to a larger diameter pipe. To perturb the flow a curved section was introduced 185D from the pipe inlet. As shown in *Figure 23D*, the differential pressure of the curved section was supervised instead of direct observation of the blood due to the characteristic opacity of the blood. Consequently, flows were deemed unsteady if deviations in pressure were larger than twice the background noise level of the sensor. Based on the conclusions of Xu *et al.* 2020 [19], like in the Newtonian flow, also the pulsatile blood flow became unstable during flow deceleration, and a considerable drag increase was detected approximately 20D downstream of the curved pipe segment while during the acceleration the flow stabilized and returned to the laminar friction value. The instability threshold for blood flow is shown by the orange symbols in *Figure 22*. In this case the transition occurs at lower  $Re_m$  than for water flows because was used a more strongly curved segment which could generate an earlier onset. For pulsation levels typical for the aorta, i.e.,  $A \approx 0.94$ , the Reynolds number threshold was as low as 800 and hence much lower than the commonly assumed value of 2000. As claimed by Xu *et al.* 2020 [19], the measurements were repeated under comparable conditions using a transparent Newtonian fluid (water), where again the deviation in pressure was used to determine the instability threshold and was found to coincide with the appearance of the helical wave (blue line in *Figure 22*).

### 2.3 TRANSIENT GROWTH NUMERICAL SIMULATIONS

Xu, Song and Avila [20] begin their study by saying that even for the simple case of pulsatile flow in a straight pipe, the mechanisms of instability and transition to turbulence are poorly understood and particularly the dependence on the pulsation amplitude is largely unknown. This makes it difficult to assess whether disturbed flow patterns in arterial and respiratory flow are solely due to geometric and structural effects (e.g. vessel curvature and flexibility, bifurcations), or are also related to the stability of pulsatile pipe flow.

It has already been stated that the pulsation amplitude  $A$ , the Womersley number  $Wo$  and the Reynolds number  $Re_s$  control the pulsatile flow in a straight pipe. It is important to note that the limit of small pulsation amplitude  $A \rightarrow 0$  (steady flow) is relevant to laminar blood flow in capillaries, whereas the opposite limit  $A \rightarrow \infty$  (oscillatory flow) is relevant to respiratory flow. It is interesting to report what was said by Kleinstreuer and Zhang [21], who stated that, in humans, the airflow may be laminar, transitional or turbulent depending on the airway segment. The intermediate regime, in which the pulsatile flow component is like the steady one ( $A \gtrsim 1$ ), is typical of blood flow in the large arteries.

In the experiments previously considered (Stettler and Hussain [8], Xu *et al.* 2017 [13] and 2020 [19]), it was found that the transition is largely anticipated, while the study of Thomas *et al.* [22] illustrated that the linear instability of oscillatory pipe flow persists also for pulsatile flow. Putting together the results obtained so far, it can be hypothesized that pulsatile pipe flow undergoes a subcritical transition to turbulence in all regimes. As found in *Sec. 2.2*, Xu *et al.* 2020 [19] reported on a nonlinear instability of pulsatile pipe flow, which occurs at pulsation amplitudes relevant for arterial flow. Furthermore, Xu *et al.* 2020 [19] performed also linear non-modal transient growth computations at a selected parameter set and showed that the most amplified disturbance is a helical wave. The relevant role of transient growth can be observed through direct numerical simulations initialized with this helical wave, that reproduced the flow patterns and the time of turbulence breakdown observed experimentally. [20]

During numerical simulations was considered an incompressible viscous fluid driven at a pulsatile flow rate in a straight pipe of circular cross-section and lengths, velocities and time are rendered dimensionless. [20]

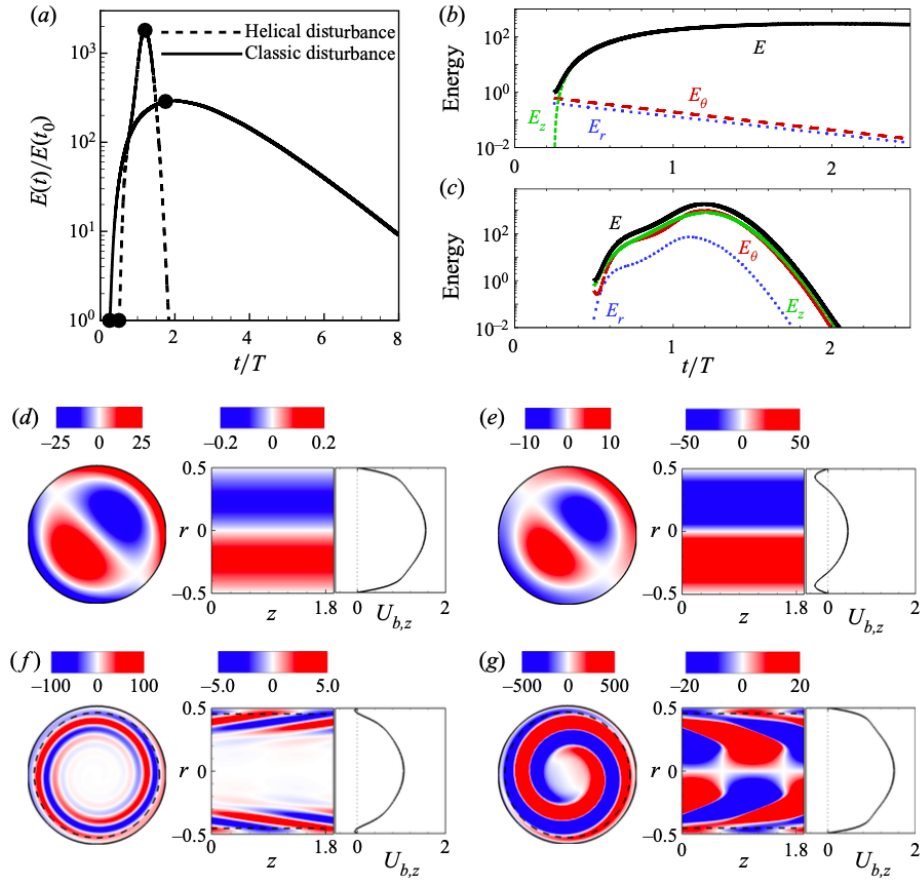
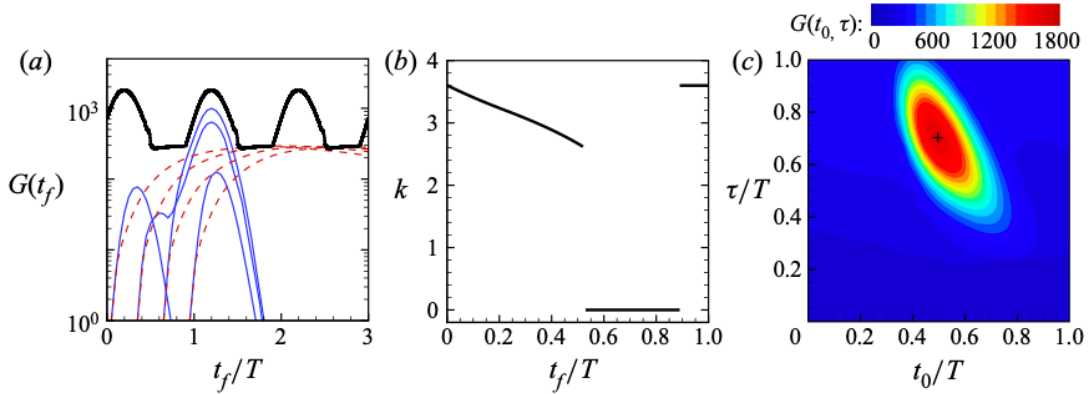


Figure 25: (a) Time series of the kinetic energy  $E(t)/E(t_0)$  of the optimal helical,  $(k, m) = (3.24, 1)$ , and classic,  $(k, m) = (0, 1)$ , disturbances at  $(Re_s, A, Wo) = (2000, 1, 15)$ . (b,c) Time series of kinetic energy contribution of each velocity component for the classic (b) and helical (c) disturbances. (d,e) Contours of stream-wise vorticity (on an  $r - \theta$  cross-section) and of stream-wise velocity (on a  $z - r$  cross-section) of the classic disturbance, and the corresponding base flow profile  $\mathbf{U}_{b,z}$  at  $t_0/T = 0.25$  (d) and  $t_f/T = 1.75$ . (f,g) The same as (d,e), but for the helical disturbance at  $t_0/T = 0.5$  and  $t_f/T = 1.2$ . The dashed line denotes the Stokes-layer thickness. [20]

Considering  $Re_s = 2000$ ,  $A = 1$  and  $Wo = 15$ , as shown in Figure 25a the temporal evolution of the optimal disturbance's energy is represented as a dashed line while in Figure 25f,g is shown that the optimal disturbance has a helical structure and is localized at the outer half of the pipe (exceeding the Stokes-layer thickness). According to Xu, Song and Avila [20], the optimal point to disturb is during the deceleration phase (at  $t_0/T = 0.5$ ), whereas the maximum amplification is reached during the acceleration phase (at  $t_f/T = 1.2$ ). As shown in Figure 25d,e, the classic disturbance initially consists of stream-wise vortices while in Figure 25b is represented that the energy is subsequently transferred to the stream-wise velocity components and the cross-stream components decay monotonically. As stated by Xu, Song and Avila [20], the classic perturbation's behavior appears to be rather insensitive to the change in flow profile throughout the cycle, and the decay is very slow.

As shown in *Figure 25c*, the kinetic energy of the optimal helical perturbation is mostly distributed in the stream-wise and azimuthal components, which self-amplify rapidly during the deceleration phase and a bit slower during the subsequent acceleration phase. Focusing on *Figure 25f*, it is clear that initially the disturbance spirals clockwise towards the pipe centre while leaning against the background shear profile. *Figure 25g* shows that as the energy grows, the perturbation switches the spiralling direction and is tilted by the shear until it aligns with it and the disturbance finally decays. Moreover, Xu, Song and Avila [20] reported a strong three-dimensional effect because approximately 96% of the kinetic energy is shared in equal parts between the azimuthal and stream-wise components.

The studies of Von Kerczek [23] and Tsigklifis & Lucey [24] both associated the modal energy growth with the inflectional velocity profiles occurring in the deceleration phase. As shown in *Figure 25f*, Xu, Song & Avila [20] stated that at the optimal perturbation point  $t_0$  the velocity profile also presents inflection points. The relevant role in pulsating pipe flow of inflection points and modal mechanisms is indicated by the results obtained in additional runs at  $Wo = 5$  and 8.



*Figure 26*: Transient growth at  $(Re_s, A, Wo) = (2000, 1, 15)$ : (a) The red dashed lines denote the temporal evolution of the optimal classic disturbances  $(k, m) = (0, 1)$  for four different initial times  $t_0$ , whereas the blue solid lines correspond to the optimal helical disturbances  $(k, m) = (3.24, 1)$  initialized at the same  $t_0$ . The thick black line is the maximum gain  $G(t_f)$  that can be achieved at a given time  $t_f$  (optimized over  $k$ ,  $m$  and  $t_0$  disturbances). (b) Dependence of the optimal axial wavenumber  $k$  (associated with the thick line of (a)) on  $t_f$ . (c) Colourmap of the maximum gain  $G(t_0, \tau)$  (optimized over  $k$  and  $m$ ) in the  $t_0 - \tau$  plane. The black cross marks the maximum of  $G$ . [20]

As shown in *Figure 26b*, the maximum amplification is reached during the acceleration phase via helical disturbances, whereas the classic disturbance achieves larger growth only during the second half of the deceleration phase. The colourmap of *Figure 26c* shows that the optimal time to perturb the flow is during the middle of the deceleration phase ( $t_0/T \approx 0.5$ ); perturbing during the acceleration phase leads to much lower growth (yielded by the classic disturbance during the deceleration phase). It is clear that the helical mechanism is efficient only in the deceleration phase. [20]

### 3. CONCLUSIONS

From the first experiments it was possible to identify three possible regimes of the transition to turbulence in pulsating pipe flow as a function of the Womersley number that specifically characterizes the transition threshold. According to Xu *et al.* 2017 [13], the three regimes are defined as follows.

- i. In the high frequency limit  $\alpha \gtrsim 12$  the transition threshold is unaffected by flow pulsation. Presumably here flow rate changes are too fast for turbulence to react and hence turbulence becomes sustained when the average Reynolds number is equal to the steady state threshold.
- ii. For low Womersley numbers ( $\alpha \lesssim 2.5$ ) the Reynolds number changes are sufficiently slow for turbulent structures to adjust to the instantaneous Reynolds number and turbulent lifetimes can be predicted by a quasi-steady assumption. Much of the expansion of turbulence occurring during the faster part of the cycle is erased once  $Re$  drops and turbulence reduces to puffs ( $Re \lesssim 2300$  Barkley *et al.* [25]). This low Reynolds number interval is critical for the survival of turbulence and the transition threshold is determined by the puff decay rates in this interval. Therefore, transition thresholds are considerably larger than in high Womersley number flows and equally transition is delayed compared to steady flow. As suggested by the quasi-steady analysis, in the low Womersley number limit the minimum Reynolds number has to be above threshold for turbulence to be sustained.
- iii. In the intermediate Womersley regime, i.e.  $2.5 \leq \alpha \lesssim 12$  the transition threshold adjusts smoothly between the two limits.

From the second experiments was reported a generic instability for pulsatile pipe flow that occurs for large pulsation amplitudes and precedes the normal turbulence transition. The helical vortex pattern characteristic for this instability sets in at unusually low Reynolds numbers. As reported by Xu *et al.* 2020 [19], weak curvature and modest pipe constrictions are sufficient to destabilize the laminar flow. In fact, curvature has a stabilizing effect under steady conditions and can even lead to relaminarization at not too large  $Re$  while constrictions, on the other hand, need to be very severe to trigger puffs in steady flow. It is interesting to note that the geometrical perturbations that appear to be most efficient in pulsatile flow are inefficient in the context of steady pipe flow and this study also shows that pulsatile flows are susceptible to qualitatively different and more subtle perturbations than steady pipe flows. Another characteristic mentioned of the identified mechanism is that the instability occurs only during part of the pulsation cycle, i.e., the deceleration, whereas acceleration relaminarizes the flow. This particular feature is shared with linear modal and non-modal mechanisms uncovered recently in pulsatile channel flow. The above findings hence suggest that pulsatile flows of sufficient amplitude, such as cardiovascular flows in large blood vessels, despite being linearly stable can periodically break down into bursts of turbulence. The responsible transition mechanism requires perturbations of finite amplitude as caused by geometrical deviations from the straight pipe case (e.g., bends or constrictions). In particular, the resulting large shear stress changes in space and time (*Figure 23C*) encountered during flow deceleration offer a possible cause for endothelial activation.

In the numerical simulations Xu, Song and Avila [20] showed that the largest transient growth in pulsatile flow of low amplitude ( $A \lesssim 0.4$ ) was produced by the classic lift-up mechanism. This result agrees with previous reported experiments of Xu *et al.* 2017 [13] (and also with the direct numerical simulations of Xu and Avila [26]), exhibiting turbulent puff and slugs as in

steady pipe flow. At higher amplitudes, helical disturbances begin to dominate in a band of intermediate Womersley number  $4 \lesssim Wo \lesssim 8$  which progressively widens toward larger  $Wo$  as the oscillatory Reynolds number  $Re_o$  is increased. It is important to underline that Xu, Song and Avila [20] considered linear transient growth of disturbances while transition to turbulence can only be completed with nonlinear effects. In fact, Xu *et al.* 2020 [19] showed that initializing direct numerical simulations with the linear optimal helical disturbance can trigger turbulent flow patterns as those observed in their experiments.

#### 4. BIBLIOGRAPHY

- [1] R. Trip, D. J. Kulik, J. Westerweel and C. Poelma, *An experimental study of transitional pulsatile pipe flow*, Phys. Fluids 24, 014103 (2012), <https://doi.org/10.1063/1.3673611>
- [2] P.D. Stein and H.N. Sabbah, *Turbulent blood flow in the ascending aorta of humans with normal and diseased aortic valves*, Circulation Res, **39**(1), 58 (1976)
- [3] R. Arina, *Fondamenti di aerodinamica*, Seconda edizione, Levrotto&Bella, Torino, 2015
- [4] F. Durst and B. Ü. L. Ünsal, *Forced laminar-to-turbulent transition of pipe flows*, J. Fluid Mech. **560**, 449 (2006)
- [5] I. J. Wygnanski and F. H. Champagne, *On transition in a pipe. Part 1. The origin of puffs and slugs and the flow in a turbulent slug*, J. Fluid Mech. **59**(2), 281 (1973)
- [6] D. J. Kuik, C. Poelma, and J. Westerweel, *Quantitative measurement of the lifetime of localized turbulence in pipe flow*, J. Fluid Mech. **645**(1), 529 (2010)
- [7] C. W. H. van Doorne and J. Westerweel, *The flow structure of a puff*, Philos. Trans. R. Soc. A **367**(1888), 489 (2009)
- [8] J. C. Stettler and A. K. M. Hussain, *On transition of the pulsatile pipe flow*, J. Fluid Mech. **170**(1), 169 (1986)
- [9] L. Yellin, "Laminar-turbulent transition process in pulsatile flow," Circulation Res. **19**(4), 791 (1966)
- [10] B. R. Ramaprian and S. W. Tu, *Fully developed periodic turbulent pipe flow. Part 2. The detailed structure of the flow*, J. Fluid Mech. **137**, 59 (1983)
- [11] R. Akhavan, R. D. Kamm, and A. H. Shapiro, *An investigation of transition to turbulence in bounded oscillatory Stokes flows Part 1. Experiments*, J. Fluid Mech. **225**, 395 (1991)
- [12] D. Bluestein and S. Einav, *Techniques in the analysis of stability of pulsatile flow through heart valves*, in Biomechanical Systems: Techniques and Applications: Cardiovascular Techniques, Vol. II, edited by C. T. Leondes (CRC Press LLC, Boca Raton, FL, 2001), pp. 4-1–4:39
- [13] D. Xu, S. Warnecke, B. Song, X. Ma and B. Hof, *Transition to turbulence in pulsating pipe flow*, J. Fluid Mech. **831**, 418-432, 2017
- [14] P. J. Florio and W. K. Mueller, *Development of a periodic flow in a rigid tube*, Trans. ASME J. Basic Engng **90** (3), 395–399, 1968
- [15] J. K. Gerrard and M. D. Hughes, *The flow due to an oscillating piston in a cylindrical tube: a comparison between experiment and a simple entrance flow theory*, J. Fluid Mech. **50** (01), 97–106, 1971

- [16] D. Samanta, A. de Lozar and B. Hof, *Experimental investigation of laminar turbulent intermittency in pipe flow*, J. Fluid Mech. **681**, 193–204, 2011
- [17] B. Hof, A. de Lozar, D. J. Kuik and J. Westerweel, *Repeller or attractor? Selecting the dynamical model for the onset of turbulence in pipe flow*, Phys. Rev. Lett. **101**, 214501, 2008
- [18] B. Hof, J. Westerwel, T. M. Schneider and B. Eckhardt, *Finite lifetime of turbulence in shear flows*, Nature **443**, 59–62, 2006
- [19] D. Xu, A. Varshney, X. Ma, B. Song, M. Riedl, M. Avila and B. Hof, *Nonlinear hydrodynamic instability and turbulence in pulsatile flow*, PNAS USA **117** 21, 11233-11239, 2020
- [20] D. Xu, B. Song and M. Avila, *Non-modal transient growth of disturbances in pulsatile and oscillatory pipe flows*, J. Fluid Mech., vol. 907, R5, 2021, doi:10.1017/jfm.2020.940
- [21] C. Kleinstreuer and Z. Chang, *Airflow and particle transport in the human respiratory system*, Annu. Rev. Fluid Mech. **742**, 254-290, 2010
- [22] C. Thomas, A. P. Bassom, P. J. Blennerhassett and C. Davies, *The linear stability of oscillatory Poiseuille flow in channels and pipes*, Phil. Trans. R. Soc. Lond., A **467**, 2643-2662
- [23] C. H. Von Kerczek, *The instability of oscillatory plane Poiseuille flow*, J. Fluid Mech. **116**, 91-114, 1982
- [24] K. Tsigklifis and A. D. Lucey, *Asymptotic stability and transient growth in pulsatile Poiseuille flow through a compliant channel*, J. Fluid Mech. **820**, 370-399, 2017
- [25] D. Barkley, B. F. Song, V. Mukund, G. Lemoult, M. Avila and B. Hof, *The rise of fully turbulent flow*, Nature **526** (7574), 550–553, 2015
- [26] D. Xu and M. Avila, *The effect of pulsation frequency on transition in pulsatile pipe flow*, J. Fluid Mech. **857**, 937-951, 2018